Sénarmont Method for Electro-Optic Effect Measurement

Andrea Pompermaier - 2053046 - andrea.pompermaier@studenti.unipd.it
Andrea Peri - 2063592 - andrea.peri.1@studenti.unipd.it

The physical phenomenon which describes the change in the refractive index of a medium under the action of an external electric field is known as the electro-optic effect. This phenomenon has a tensorial nature so that an external electric field produces different changes in the refractive index ellipsoid depending on its direction. The perturbation of the impermeability tensor, which depends linearly on the applied electric field, is known as Pockels effect. Only non-centrosymmetric crystals may have Pockels effect. This is the case of Lithium Niobate ($LiNbO_3$), one of the most popular electro-optic crystals. It finds many technological applications in different fields, from communications and information processing to quantum computing, since it allows to modulate and impose information on a light wave carrier. Some of the most important applications are for example the optical modulators, polarization controllers and different types of sensors [1].

This experiment consists in the measurement of the electro-optic coefficient r_{22} induced in a $LiNbO_3$ sample, with dimensions of $4 \times 4 \times 24 mm^3$, by an external oscillating electric field. A frequency analysis is useful not only to evaluate the variation of the birefringence induced in the crystal at different frequencies, but it is also an effective method to filter noise. The experimental apparatus consists in an optical setup based on the Sénarmont method with a Uniphase He-Ne laser source at wavelength $\lambda = 543.5 nm$. With this setup the coefficient r_{22} is related to the intensity variation of the beam which can be measured with photodiodes and a suitable electronic system designed to properly detect small noisy signals.

The report is organized as follows: Section **I** contains the theoretical description of the electro-optic effect, followed by a discussion on the Sénarmont method for the measurement of the r_{22} electro-optic coefficient of the crystal. In this experiment two types of detectors are employed to describe the properties of the beam: a photodiode SM1PD1A and an Omnivision CMOS CCD sensor. The first is used to measure the intensity of the beam and its characterization is described in Section **II**. The CCD sensor, described in Section **III**, is a useful instrument to measure the beam waist and characterize the laser beam profile (Section **IV**). In Section **V** we discuss the choice of the experimental design and the way we realized it. The final electronic device for data acquisition, which has been accomplished only after completing the optical line, is described in Section **VI**. Finally, in Section **VII** we discuss the data analysis method and the obtained results.

CONTENTS

I. INTRODUCTION

The purpose of this chapter is to provide the theoretical basis on which the entire experiment is based. In particular, in Sec. I.1 we provide a description of the electro-optic effect with particular regard to the linear effect (also known as the Pockels effect). In Sec. I.2 we describe the Sénarmont method and some theoretical relations which will later become fundamental for the estimation of the electro-optic coefficient r_{22}.

1. Birefringence and electro-optic effect

The electro-optic effect describes the modification of the dielectric tensor of a material in response to an applied electric field $\mathbf{E}$. This phenomenon depends on the microscopic structure of the medium: the electric field induces a slight displacement of the atomic charges and consequently a non-zero dipole moment. Anisotropic media, like $LiNbO_3$, are materials in which the dipole moment, and therefore the dielectric displacement $\mathbf{D}$, depends on the direction as well as the magnitude of the applied electric field vector $\mathbf{E}$ [2]. Here we assume that the material polarization linearly depends on the applied electric field since we are interested in studying the Pockels effect of $LiNbO_3$. The dielectric displacement can be written as follows:

$$\mathbf{D}(\omega) = \epsilon_0 \mathbf{E}(\omega) + \mathbf{P}(\omega) = \epsilon_0 (1 + \hat{\chi}(\omega))\mathbf{E}(\omega) = \epsilon_0 \hat{\epsilon}(\omega)\mathbf{E}(\omega) \tag{1}$$

where $\hat{\chi}(\omega)$ is the electric susceptibility tensor, which strictly depends on the symmetry properties of the medium, and ϵ_0 is the vacuum dielectric constant. Within the medium the dielectric displacement depends on the properties of the material via the relative dielectric tensor $\hat{\epsilon}(\omega) = 1 + \hat{\chi}(\omega)$. This quantity depends not only on the symmetry properties of the material, but also on the amplitude and frequency of the applied electric field.

The $LiNbO_3$ crystal has a trigonal unit cell which is invariant under rotations of $120°$ about the optical axis (conventionally indicated as z-axis). By exploiting the properties of the lattice structure, one can demonstrate that the relative dielectric tensor, in the absence of external electric fields, is diagonal [2]:

$$\hat{\epsilon} = \begin{pmatrix} \epsilon_{xx} & 0 & 0 \\ 0 & \epsilon_{yy} & 0 \\ 0 & 0 & \epsilon_{zz} \end{pmatrix} = \begin{pmatrix} n_o^2 & 0 & 0 \\ 0 & n_o^2 & 0 \\ 0 & 0 & n_e^2 \end{pmatrix} \tag{2}$$

where we denote n_o the ordinary refractive index (along the x and y-axis) while n_e is the extraordinary refractive index (along the z-axis).

In the literature typically Eq. 1 is expressed in terms of the impermeability tensor $\hat{b}$ in the following way:

$$\mathbf{E} = \frac{1}{\epsilon_0}\hat{\epsilon}^{-1}\mathbf{D} = \frac{1}{\epsilon_0}\hat{b}\mathbf{D} \tag{3}$$

The presence of an external electric field $\mathbf{E} = (E_x, E_y, E_z)$ (the components are expressed in the same reference frame of the crystal), as previously mentioned, alters the impermeability tensor components. To describe quantitatively the variation of the impermeability tensor $\Delta\hat{b}$ induced by an external electric field we introduce the electro-optic tensor $\hat{r}$:

$$b_{ij} = b_{ij}^{(0)} + \Delta b_{ij} \qquad\qquad \Delta b_{ij} = \sum_k r_{ijk} E_k \tag{4}$$

where $\hat{b}^{(0)}$ denotes the impermeability tensor in the absence of an external electric field. The linear electro-optic effect (Pockels effect) is described by the third rank tensor $\hat{r}$, which is invariant under the permutation $r_{ijk} = r_{jik}$, $i, j, k = 1, 2, 3$, since $\Delta b_{ij} = \Delta b_{ji}$. Therefore the residual 18 degrees of freedom of the tensor can be represented by a 6×3 matrix: $r_{ijk} \Rightarrow r_{ij}$ [1]. With this representation we can rewrite the 6 possible variations of the impermeability tensor $\Delta b_{ij} \Rightarrow \Delta b_i$ in the following way:

$$\begin{pmatrix} \Delta b_1 \\ \Delta b_2 \\ \Delta b_3 \\ \Delta b_4 \\ \Delta b_5 \\ \Delta b_6 \end{pmatrix} = \begin{pmatrix} r_{11} & r_{12} & r_{13} \\ r_{21} & r_{22} & r_{23} \\ r_{31} & r_{32} & r_{33} \\ r_{41} & r_{42} & r_{43} \\ r_{51} & r_{52} & r_{53} \\ r_{61} & r_{62} & r_{63} \end{pmatrix} \begin{pmatrix} E_1 \\ E_2 \\ E_3 \end{pmatrix} \qquad\qquad \hat{b} = \begin{pmatrix} b_o + \Delta b_1 & \Delta b_6 & \Delta b_5 \\ \Delta b_6 & b_o + \Delta b_2 & \Delta b_4 \\ \Delta b_5 & \Delta b_4 & b_e + b_3 \end{pmatrix} \tag{5}$$

From the lattice structure properties [1], it is possible to derive the electro-optic tensor for the $LiNbO_3$:

$$\hat{r} = \begin{pmatrix} 0 & -r_{22} & r_{13} \\ 0 & r_{22} & r_{13} \\ 0 & 0 & r_{33} \\ 0 & r_{51} & 0 \\ r_{51} & 0 & 0 \\ -r_{22} & 0 & 0 \end{pmatrix} \implies \hat{b} = \begin{pmatrix} b_o - r_{22}E_y + r_{13}E_x & -r_{22}E_x & r_{51}E_x \\ -r_{22}E_x & b_o + r_{22}E_y + r_{13}E_z & r_{51}E_y \\ r_{51}E_x & r_{51}E_y & b_e + r_{33}E_z \end{pmatrix} \tag{6}$$

In case of an electric field applied along the y-direction ($E_x = E_z = 0$), the impermeability tensor becomes:

$$\hat{b} = \begin{pmatrix} b_o - r_{22}E_y & 0 & 0 \\ 0 & b_o + r_{22}E_y & r_{51}E_y \\ 0 & r_{51}E_y & b_e \end{pmatrix} \sim \begin{pmatrix} b_o - r_{22}E_y & 0 & 0 \\ 0 & b_o + r_{22}E_y & 0 \\ 0 & 0 & b_e \end{pmatrix} \tag{7}$$

where $b_o = \frac{1}{n_0^2}$ and $b_e = \frac{1}{n_e^2}$. The off-diagonal elements indicate that the index ellipsoid is tilted by an angle along y-z directions, however this contribute is quite small and for our analysis can be neglected. From Eq. 7 we deduce that the action of an electric field along the y-axis induces a birefringence in the crystal along the x and y-axis which depends on the r_{22} coefficient.

The refractive index along the x-axis is:

$$\frac{1}{n_x^2} = b_o - r_{22}E_y \implies n_x = n_o(1 - n_o^2 r_{22}E_y)^{-1/2} \sim n_o\left(1 + \frac{n_o^2 r_{22}E_y}{2}\right) \tag{8}$$

where the last result has been obtained by a first order Taylor expansion. Similarly we obtain the refractive index along the y-axis:

$$\frac{1}{n_y^2} = b_o + r_{22}E_y \implies n_y \sim n_o\left(1 - \frac{n_o^2 r_{22}E_y}{2}\right) \tag{9}$$

The experimental quantity that we can measure is the difference between these two refractive indexes:

$$\Delta n_{xy} = n_x - n_y = n_0^3 r_{22}E_y \tag{10}$$

which depends linearly on the electric field applied along the y-axis E_y.

2. The Sénarmont method

The birefringence induced in the crystal along the x and y-axis (Eq. 10) by the external electric field can be measured with the Sénarmont method. This method allows to estimate the relative phase retardation induced by the crystal between the components x and y of a linearly polarized optical beam propagating along the z-direction (see Fig. 1). The initial beam is linearly polarized at 45° with respect to the x-axis (from now on if not specified we will implicitly assume the reference frame of the crystal). After passing through the sample, the components of the beam along the x and y-axis undergo a change in their relative phase (δ) and the final polarization of the beam becomes elliptical (with the principal axis oriented at 45°). The outgoing beam passes through a $\lambda/4$ waveplate with its fast axis oriented at 45° which removes the phase shift of $\pi/2$ between the two components in the waveplate reference frame. The final beam is linearly polarized, with an angle $\gamma = -\delta/2$ in the waveplate reference frame.

The Sénarmont method can be demonstrated using the Jones calculus. The linearly polarized at 45° incoming beam is denoted as follows:

$$E = \frac{1}{\sqrt{2}}\begin{pmatrix} 1 \\ 1 \end{pmatrix} \tag{11}$$

The beam passes the birefringent crystal which induces two different phases along the components x (ϕ_x) and y (ϕ_y) depending on the corresponding refractive index, the length of the crystal L, and the wavelength λ. The relative phase is denoted as $\delta = \phi_x - \phi_y$. This process is described by the Jones matrix $T_{crystal}$ defined as follows:

$$T_{crystal} = \begin{pmatrix} e^{i\phi_x} & 0 \\ 0 & e^{i\phi_y} \end{pmatrix} = \begin{pmatrix} e^{\frac{i2\pi}{\lambda}Ln_x} & 0 \\ 0 & e^{\frac{i2\pi}{\lambda}Ln_y} \end{pmatrix} = \begin{pmatrix} e^{\frac{i2\pi}{\lambda}L\Delta n_{xy}} & 0 \\ 0 & 1 \end{pmatrix} = \begin{pmatrix} e^{i\delta} & 0 \\ 0 & 1 \end{pmatrix} \tag{12}$$

Then the beam passes through the $\lambda/4$ waveplate (with fast axis at 45°). The corresponding Jones matrix $T_{\lambda/4}^{45°}$ is the following:

$$T_{\lambda/4}^{45°} = R(-45°)T_{\lambda/4}R(45°) = \frac{1}{2}\begin{pmatrix} 1 & 1 \\ -1 & 1 \end{pmatrix}\begin{pmatrix} 1 & 0 \\ 0 & -i \end{pmatrix}\begin{pmatrix} 1 & -1 \\ 1 & 1 \end{pmatrix} = \frac{1}{2}\begin{pmatrix} 1-i & -1-i \\ -1-i & 1-i \end{pmatrix} \tag{13}$$

$T_{\lambda/4}^{45°}$ is obtained by rotating of 45° the Jones matrix corresponding to a waveplate with the fast axis oriented along the x-direction.

Finally, we find that the outcoming beam is elliptically polarized in the state E' which is obtained by combining the previous two transformations:

$$E' = T_{\lambda/4}^{45°}T_{crystal}E = \frac{1}{2\sqrt{2}}\begin{pmatrix} e^{i\delta} - ie^{i\delta} & -1-i \\ -e^{i\delta} - ie^{i\delta} & 1-i \end{pmatrix}\begin{pmatrix} 1 \\ 1 \end{pmatrix} = \frac{1}{2\sqrt{2}}\begin{pmatrix} -1-i+e^{i\delta}-ie^{i\delta} \\ 1-i-e^{i\delta}-ie^{i\delta} \end{pmatrix} \tag{14}$$

Now, we pass to the waveplate reference frame by applying a rotation of $-45°$ to the state E' (in this new system the x-axis coincides with the fast axis of $\lambda/4$ waveplate). This state in the waveplate reference frame is denoted as E'':

$$E'' = R(-45°)E' = \frac{1}{4}\begin{pmatrix} 1 & 1 \\ -1 & 1 \end{pmatrix}\begin{pmatrix} -1-i+e^{i\delta}-ie^{i\delta} \\ 1-i-e^{i\delta}-ie^{i\delta} \end{pmatrix} = \frac{1}{2}\begin{pmatrix} -i-ie^{i\delta} \\ 1-e^{i\delta} \end{pmatrix} = \frac{1}{2}\begin{pmatrix} -i-icos\delta+sin\delta \\ 1-cos\delta-isin\delta \end{pmatrix} = \begin{pmatrix} |E_1|e^{i\theta_1} \\ |E_2|e^{i\theta_2} \end{pmatrix} \tag{15}$$

It is easy to show that in this new reference frame the outcoming beam E'' is linearly polarized since the two phases are the same.

$$\begin{cases} |E_1| = \sqrt{\frac{1+cos\delta}{2}} \\ |E_2| = \sqrt{\frac{1-cos\delta}{2}} \end{cases} \qquad \begin{cases} tg\theta_1 = -\frac{1+cos\delta}{sin\delta} \\ tg\theta_2 = -\frac{sin\delta}{1-cos\delta} \end{cases} \qquad \Rightarrow \qquad tg\theta_1 = tg\theta_2 = -\sqrt{\frac{1+cos\delta}{1-cos\delta}} \tag{16}$$

The polarization angle γ of the state E'' in the $\lambda/4$ waveplate reference frame is:

$$tg\gamma = \frac{|E_2|}{|E_1|} = \sqrt{\frac{1-cos\delta}{1+cos\delta}} = \pm tg\left(\frac{\delta}{2}\right) \tag{17}$$

The sign depends on the direction of the rotation of the elliptically polarized state E'(+ for counterclockwise and - for clockwise) which depends on the phase difference induced by the crystal on the x and y components of the initial state E. Since we don't know *a priori* the magnitude of this phase shift both directions are in principle allowed. Moreover, as we will discuss in Sec. **V** we cannot experimentally distinguish the state of polarization of the incoming beam between $+45°$ and $-45°$ and the same argument holds also for the $\lambda/4$ waveplate. The Sènarmont method, in any case, allows to estimate the amplitude of this angle independently of its sign. For the following discussion, we can arbitrarily fix this angle to $\gamma = -\frac{\delta}{2}$ and the phase shift induced by the crystal (Eqs. 10 and 12) can be written as:

$$\delta = \frac{2\pi}{\lambda}L\Delta n_{xy} = \frac{2\pi}{\lambda}Ln_o^3r_{22}E_y \tag{18}$$

The final linearly polarized beam can be analyzed using a polarizer (further called analyzer). The intensity detected as a function of the polarizer angle θ is:

$$I(\theta) = I_0cos^2(\theta - \gamma) = \frac{I_0}{2}[1 + cos(2(\theta - \gamma))] \tag{19}$$

Thus, by setting the polarizer angle at $\theta = 45°$, since δ is a small quantity, we can approximate the previous equation through a Taylor expansion in the following way:

$$I\left(\frac{\pi}{4}\right) = \frac{I_0}{2}\left[1 + cos\left(2\left(\frac{\pi}{4} + \frac{\delta}{2}\right)\right)\right] \sim \frac{I_0}{2}(1 - \delta) = \frac{I_0}{2}(1 - \frac{2\pi}{\lambda}Ln_0^3r_{22}E_y) \tag{20}$$

If we set an oscillating electric field $E_y = \frac{V}{d}$ (where d is the sample thickness and V the applied voltage) it is possible to relate the amplitude of the light intensity oscillations ΔI in the linear regime to the applied voltage:

$$\frac{\Delta I}{I_0} = -\frac{\pi}{\lambda}Ln_0^3r_{22}\frac{V}{d} \tag{21}$$

We observe that all the quantities in Eq. 21 are known except I_0. This quantity can be estimated through a linear regression of the intensities measured for θ close to $\pi/4$ in the absence of an external electric field. Indeed, setting $\Delta\theta = \theta - \pi/4$, we have:

$$I(\Delta\theta) = I_0 cos^2(\Delta\theta + \pi/4) = \frac{I_0}{2}[1 + cos(2(\Delta\theta + \pi/4))] \sim \frac{I_0}{2}(1 - 2\Delta\theta) = \frac{I_0}{2} - I_0\Delta\theta \tag{22}$$

Close to $\theta = \pi/4$ the intensity of the beam depends linearly on the phase difference $\Delta\theta$ and the angular coefficient is I_0. Inserting this result in the Eq. 21, it is possible to estimate the electro-optic coefficient r_{22}. We have to take into account that the linear approximation holds only for small variations of the phase $\Delta\theta$ (or equivalently to the phase γ in presence of an electric field). The limits of this approximation will be described in more detail in Sec. **VII**.
From these relations it is possible to see that the only effect of the sign of γ as well as the choice of setting the polarization of the incident beam at $\pm 45°$ is on the sign of the slope, not its magnitude (on which r_{22} depends).
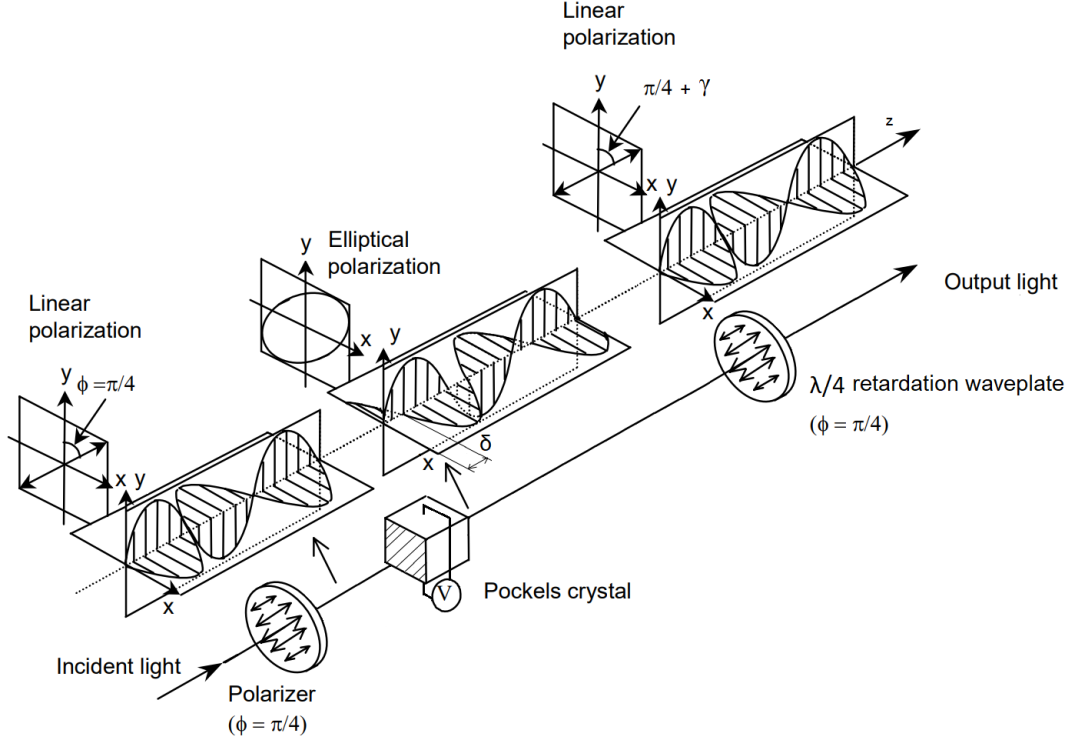

FIG. 1. Schematic of the three different polarization states of the beam in the Sénarmont method. The incoming photons are linearly polarized at $45°$. After the sample the two components acquire a relative phase δ and the polarization is elliptical (with major axis at $45°$). Finally, the $\lambda/4$ waveplate restores the linear polarization with an angle of $45° + \gamma$. (modified from [3])

II. PHOTODIODE CHARACTERIZATION

The key point for estimating the electro-optic coefficient r_{22} using the Sénarmont method consists in measuring the small variations in light intensity induced by the combination of the birefringence of the crystal, the effect of the $\frac{\lambda}{4}$ waveplate and the analyzer. For this purpose, we used the photodiode **SM1PD1A** (datasheet), which is sensitive to low intensity light signals with a wavelength in the range $350 - 1100$ nm. This detector, when it absorbs light with the right frequency, produces a current proportional to the power of the incident light beam. The responsivity of the photodiode is a measure of its sensitivity to light and it is defined as the ratio between the photocurrent i_d and the power P of the incident light at a given wavelength λ:
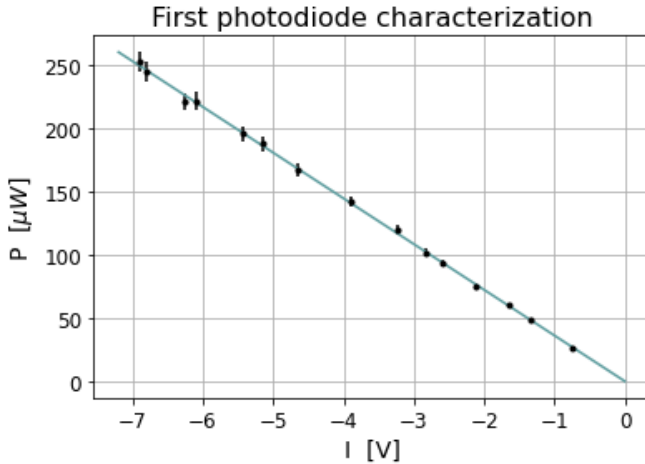
$$R_\lambda = \frac{i_d}{P} \tag{23}$$

Knowing the wavelength of the laser beam ($\lambda = 543.5nm$), it is possible to estimate the corresponding responsivity of the instrument: $R_{543.5nm} \sim 0.23 A/W$ (this approximated result has been deduced by the graph of the responsivity as a function of the wavelength found in the datasheet and shown in Fig. 2). Given the power of the incident light, which can be measured using a power meter, we can estimate the induced photocurrent i_d. This current is fed into a transimpedance amplifier, which outputs a voltage V_{out} that is proportional to the input current (Fig. 3).

$$V_{out} = -R\, i_d$$

The resistor R can be adapted to change the gain of the circuit for a given input photocurrent. The output voltage V_{out} is proportional to the power of the incident light per unit area of the detector (from now on it will be used as a measure of the light intensity). In the first realization of the transimpedance amplifier, we used a resistance $R = (118.4 \pm 0.2)k\Omega$ to obtain a high gain from the transimpedance amplifier, thus a high resolution in measuring small current signals. We noted that such a high resistance is associated with severe thermal fluctuations which cause a high electronic noise in the output voltages. This problem can be partially solved by setting the oscilloscope to display an averaged signal: with this configuration we observed an $RMS \sim 20mV$. Another issue pertaining the presented electronic device is the temporal instability caused by the laser beam power fluctuations. To limit the effect of these issues a new electronic circuit, designed mainly for the measurement process, will be described in Sec. VI.

The characterization of the linear response of the apparatus has been achieved by means of two polarizers positioned just in front of the photodiode in order to vary the light power by changing the polarization axis of one of them (from Malus' law).

FIG. 2. Responsivity of SM1PD1A photodiode as a function of the wavelength of the incident light (taken from datasheet).
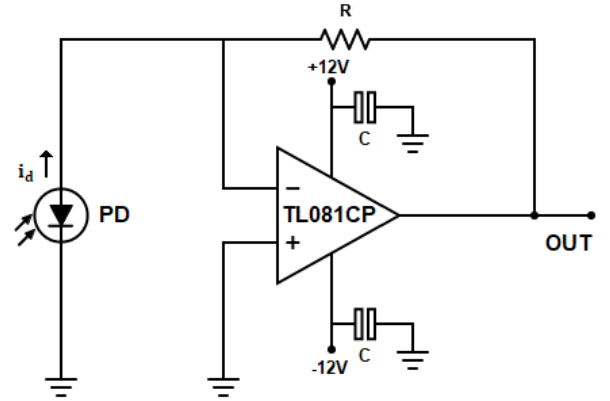
FIG. 3. Schematic representation of a transimpedance amplifier. We used the OPAMP **TL081CP** (datasheet).

For each configuration of the polarizers, we measured the light power recorded by a power meter and we plot it as a function of the output voltage of the transimpedance amplifier (Fig. 4a). The results follow a linear trend, confirmed by the Pearson coefficient $r = -0.9997$.

(a) Photodiode characterization. We obtain an angular coefficient $m = (-36.2 \pm 0.2)\mu W/V$
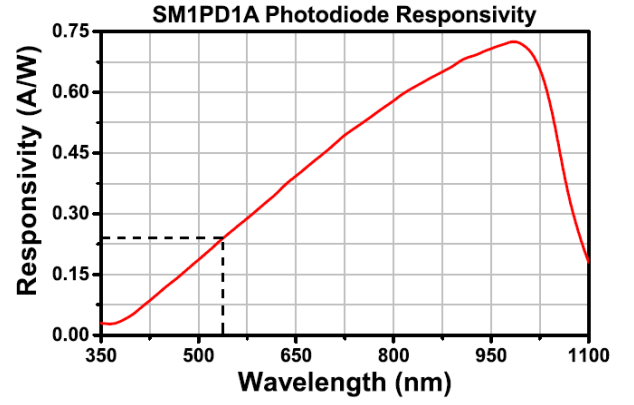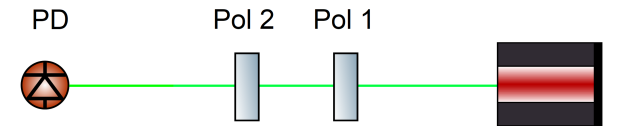

(b) Experimental setup for the photodiode characterization

FIG. 4

III. CMOS SENSOR CHARACTERIZATION AND CALIBRATION

Before building the appropriate optical setup, we need to characterize the properties of the laser beam. This procedure requires an instrument capable of acquiring beam section images. For this experiment we used a **Omnivision** CMOS sensor. This CCD sensor can be used to acquire images of the beam sections in three different channels (Red, Blue and Green); given the wavelength $\lambda = 543.5nm$ of the He-Ne laser we have, we are only interested in the results concerning the green component of the acquired data. Raw data are stored in a matrix for each color containing the light intensity recorded by each pixel as a number from 0 to 256. The data files can be managed with a proper software (*Micro-Manager*) through which it is possible to analyze the stored images in each of the three channels separately. In the following two sections we will deal with two fundamental quantities necessary for the analysis that will be discussed in Sec. **IV** and **V**: the intensity calibration of the CMOS sensor (Sec. **III.1**) and the estimation of the pixel size (Sec. **III.2**).

1. Intensity calibration

The response of the CCD as a function of the intensity of the incident light is not linear and depends both on the wavelength and the energy of the incoming radiation: a proper calibration of the CCD is necessary to accurately measure the 2D intensity beam profile. For this scope, we used our photodiode with the transimpedance amplifier (which, as discussed in Sec. **II**, has a linear response as a function the incoming light power).
The 2D intensity profile of an ideal gaussian beam is defined as follows:

$$I(x,y) = Ae^{-2\frac{x^2+y^2}{W^2}} \tag{24}$$

where A is the amplitude (corresponding to the maximum value of the intensity) and W is the beam waist. The CCD has a non-linear response which can be typically described by the following function:

$$I_{CCD} = I_{real}^{\gamma} \tag{25}$$

where γ is a parameter that must be experimentally estimated and I_{real} is the true measured intensity.
The intensity calibration can be performed by comparing the values measured by means of the CCD with some reference values. For the reference we used the photodiode, which reveals a voltage signal V proportional to the intensity I_{tot} of the whole beam, which is given by integrating the 2D intensity function defined in Eq. **24**:

$$I_{tot} = \frac{\pi}{2}W^2A \tag{26}$$

This formula states that the intensity of the beam I_{tot} revealed with the photodiode is proportional to the maximum value of the intensity of the beam (A). This quantity can be experimentally estimated through the images of the beam section acquired with the CCD.
The calibration consists in measuring the maximum value of the intensity recorded with the CCD and the total intensity of the beam through the photodiode. In Fig. **5b** the experimental apparatus is shown: two polarizers Pol1 and Pol2 set the intensity of the beam by changing the orientation of Pol1 keeping fixed Pol2. The photodiode and the CCD are positioned at the ends of the two branches of a 50:50 beam splitter. To avoid the CCD saturation, which would prevent the correct determination of the intensity peak, we introduced in front of the CMOS sensor a set of three absorptive density filters with optical densities 1, 0.4, and 0.3; in this way the intensity is reduced of a factor $10^{1.7}$. The sensors has been shielded from the environmental background with a tube put just in front of the detectors. The residual background (obtained with an acquisition with the laser off) is not zero and presents a mean value of ~ 10 arbitrary units.
We collected data regarding the maximum value of the intensity measured with the CCD (I_{CCD}) and the total intensity measured with the photodiode (I_{PD}). In (Fig. **5a**) we plotted I_{CCD} vs I_{PD} and fitted the data with the following function:

$$I_{CCD} = I_{CCD}^{(0)} + K(I_{PD} - I_{PD}^{(0)})^{\gamma} \tag{27}$$

where $I_{PD}^{(0)} = (44 \pm 5)mV$ is the intensity measured with the photodiode when the laser is turned off: it is due to environmental light. $I_{CCD}^{(0)} = 8.3 \pm 0.8$ is the environmental background detected by the CCD (expressed in terms of the arbitrary units of the instruments). As expected, the CCD saturates for high intensities. The fundamental

parameter for the calibration is the exponent $\gamma = 0.59 \pm 0.02$, which describes how the CCD response deviates from linearity.
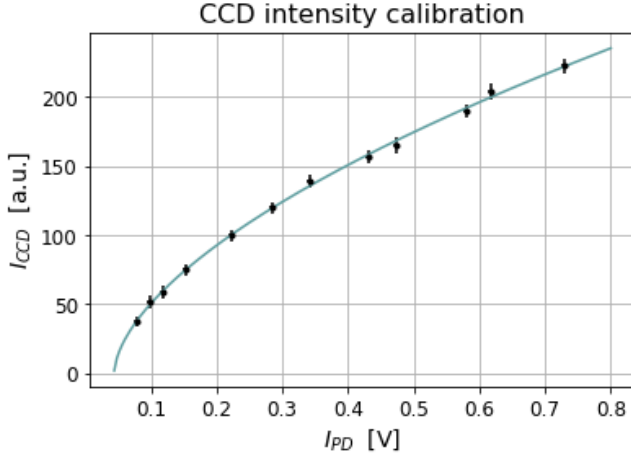
(a) CCD intensity calibration
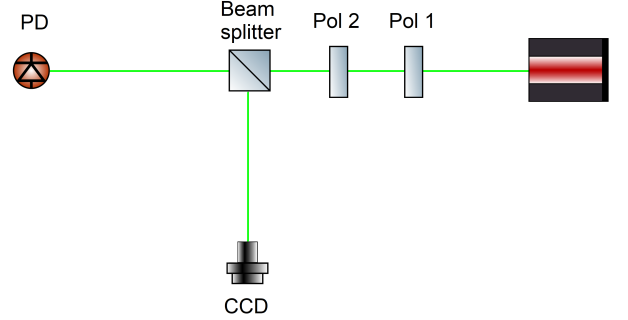
(b) Experimental setup for the CCD intensity calibration

FIG. 5. In Fig. 5a the maximum value of the 2D gaussian beam profile is plotted as a function of the intensity measured with the photodiode. The experimental setup employed for these measurements is presented in Fig. 5b.

The results of this calibration are necessary to correctly determine the intensity profile of the images acquired with this instrument and their corresponding waists. The purpose of this analysis is to convert the intensity measured by the CCD into a quantity proportional to the real one, this can be done considering:

$$I_{real} \propto (I_{meas} - I_0)^{1/\gamma} \tag{28}$$

where, for our purposes, we are not directly interested in the proportionality constant.
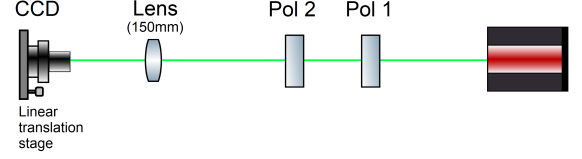
2. Pixel size estimation

The laser beam profile characterization requires an accurate estimation of the beam waist. This quantity is experimentally measured using the images acquired with the CCD which has a spatial resolution corresponding to the pixel size. In this section we will discuss a simple method to estimate the actual value of this quantity for our CCD sensor. We modified the experimental setup (see Fig. 6b) by removing the beam splitter from the previous apparatus. The CCD was mounted on a linear translational stage which is able to move horizontally the detector along the transversal direction with respect to the optical axis. The position of the CCD can be regulated with a micrometric screw with resolution $0.02mm$. The laser beam was focalized with a lens with focal length 150 mm in order to reduce as much as possible the size of the incident beam on the detector. To avoid intensity saturation of the CCD, due to the highly focused beam, we introduced an additional absorptive density filter (with density 2.0) and we set the polarizers Pol1 and Pol2 in a suitable configuration to detect the maximum intensity without saturation. We set the CCD in different horizontal positions (X_{CCD}) and for each of them we determined the horizontal position of the beam center (in the image provided by the CCD) in pixel units (X_{pixel}). Since the beam is highly focused we estimated an uncertainty of 2 pixels in the measurements of X_{pixel}. The pixel size (m) is directly estimated through the slope of a linear fit (see Fig. 6a):

$$X_{CCD} = mX_{pixel} + q \tag{29}$$

The estimated pixel size is $m = (5.00 \pm 0.01)\mu m$.
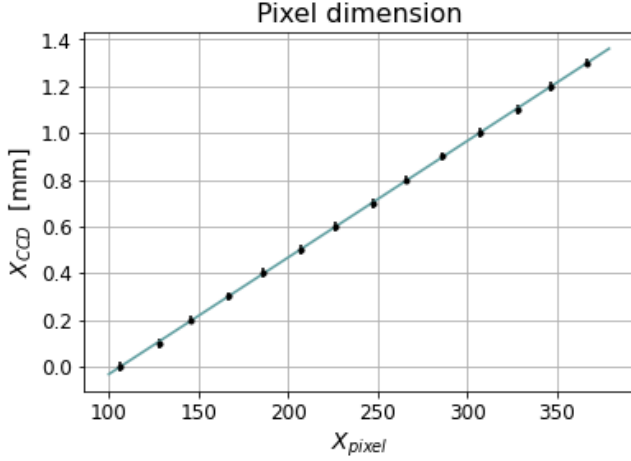
(a) Linear fit for pixel size estimation

(b) Experimental setup for pixel size estimation

FIG. 6. In Fig. **6**a it is presented the plot of the CCD position as a function of the beam center. The experimental setup employed for these measurements is presented in Fig. **6**b.

IV. LASER BEAM CHARACTERIZATION

In this section we will analyze the characteristics of the He-Ne laser source **UniPhase 1652** (datasheet). The datasheet states that this laser provides an optical beam with wavelength $\lambda = 543.5 nm$ and a maximum output power $P_0 = 4 mW$. Actually, we verified that the power provided by the laser is smaller than the quantity declared by the producer, as we discuss in Sec. **IV.2**.

This type of characterization will be fundamental for the design of the optical line (Sec. **V**) and the electronic system for data acquisition (Sec. **VI**). We start by discussing the parameters related to the beam propagation (Sec. **IV.1**) and then we will analyze the fluctuations in the beam power emitted by the laser (**IV.2**) and in its polarization (**IV.3**).

1. Beam parameters

A real gaussian beam has a waist $W(z)$ which changes depending on the position along the beam axis (z), accordingly with the following relation:

$$W(z) = W_0^{(M)} \sqrt{1 + \left(\frac{z - z_0}{z_R}\right)^2} \qquad (30)$$

where z_0 is the position of the beam focus, $W_0^{(M)}$ the waist in such position and z_R is the Rayleigh length. M^2 is a factor which takes into account the possibility that other spatial modes apart from the gaussian one may be transmitted. Since the minimum waist is defined as $W_0^{(M)} = \sqrt{\frac{\lambda z_R}{\pi} M^2}$ and the wavelength is known, the only free parameters to estimate are z_0, z_R and M^2.

We measured the beam waist $W(z)$ using the CCD at different distances with respect to the laser exit point

FIG. 7. Plot of the estimated beam waist as a function of the distance.

(considered as $z = 0$ in our reference frame). For each position, we acquired an image of the beam section and we get two estimations of the waist (along the x and y-axis) by fitting with a gaussian the corresponding sections. Since the beam is not perfectly gaussian, the two estimations are slightly different. For this reason, in each configuration, we
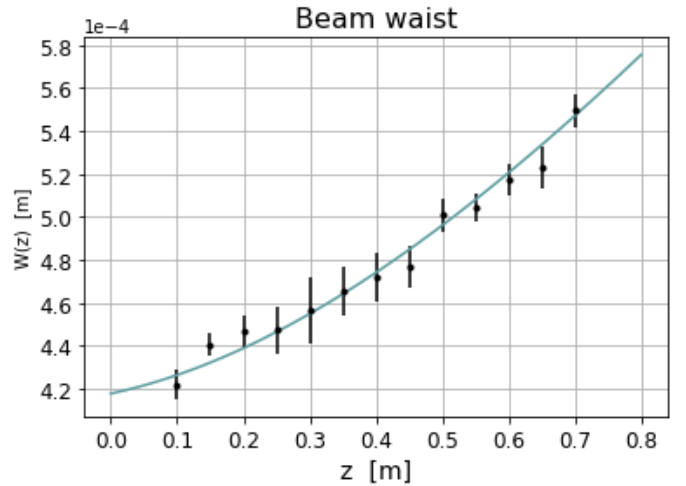
estimate $W(z)$ as the average between the two estimated waists along the x and y-axis. The results (in Fig. 7) are fitted using Eq. 30.

$$z_0 = (-0.16 \pm 0.02)m \qquad\qquad z_R = (0.98 \pm 0.02)m \qquad\qquad M^2 = 1.05 \pm 0.04$$

The uncertainties in the plot of Fig. 7 depend on the difference between the two estimations of the waist obtained for each configuration. The Rayleigh length obtained with this plot is perfectly compatible with the one declared by the producer and also the M^2 factor is compatible with our expectations ($M^2 \sim 1.1$ for He-Ne laser sources). We are mainly interested in the parameter z_R since it defines the Rayleigh range (the region in which the laser beam is approximately collimated) and the divergence of the beam $\left(\theta^{(M)} = \frac{W_0^{(M)}}{z_R}\right)$. Since the area of our detectors is finite and we would like them to collect all the beam power at every distance from the laser source, we need to keep the beam waist smaller than approximately six times the radius of the active detector surface. This will be done using a lens, and the estimation of the Rayleigh parameter can give us hints on the type of lens to be used and the position at which insert it.

2. Laser power fluctuations

Once turned on, the laser source takes about 10/15 minutes to warm up and stabilize: during this phase an increase in the light power of the beam is observed accompanied by large fluctuations. In addition, the laser source is not ideal and it exhibits some unpredictable behaviors. We observed that in the operating regime the beam power fluctuates: these fluctuations are quantified as $\sim 4\%$ of the mean intensity. Moreover, the mean power can systematically change during longer time intervals due, for example, to the overheating of the source. These issues can represent a problem in the time period in which we perform the measurements needed to estimate the r_{22} electro-optic coefficient, since the power of the beam at the end of the optical line is the main quantity we are interested in. In Fig. 8 it is shown the trend of the power emitted by the laser over a 17 minutes time window in the operating regime. We need to consider this phenomenon in the design of the electronic system. A simple way to deal with this behavior is to insert in the Sénarmont apparatus a beam splitter and a photodiode in one of its branches which will act as a reference of the beam power (see Fig. 10). In Sec. V and VI we will provide a complete description of this choice.
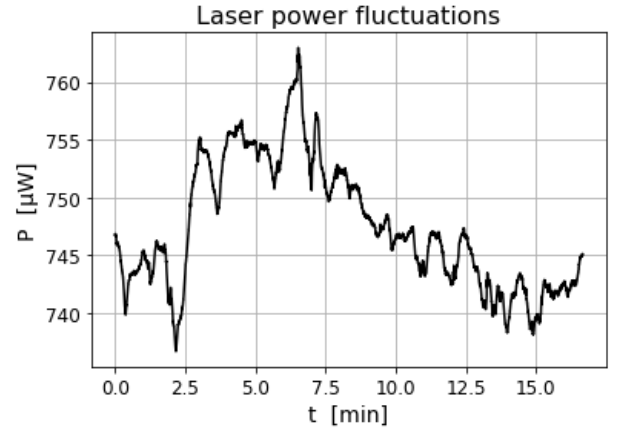

FIG. 8. Typical laser light power fluctuations recorded over a 17 minutes time window. We measured a mean intensity $\bar{I} = (747.42 \pm 0.04)\mu W$ and intensity fluctuations $\sim 4\%$.

3. Laser polarization fluctuations

Another phenomenon consists in the temporal fluctuations of the beam polarization. We initially assumed the presence of such fluctuations in the design of the optical line, and we finally observed them after building the entire electronic apparatus. While a complete description will be carried out in the next chapter, the main idea of the optical setup consists in a slight modification of the basic Sénarmont apparatus by splitting the laser beam with a 50:50 beam splitter. One of the two branches of the laser beam is directed toward the first polarizer (which prepares the polarization state at the input of the crystal), while the other one is directed to a second photodiode which collects and measures the beam power
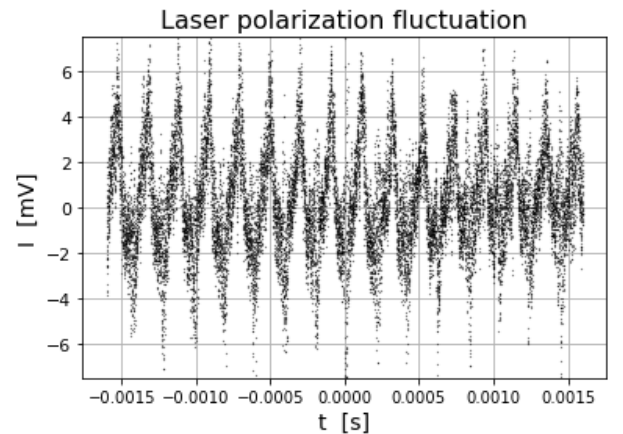

FIG. 9. Laser polarization fluctuations recorded with the oscilloscope in the AC mode.

and acts as a reference. What we noticed with this setup is that in general the signal recorded by the photodiode at the end of the optical line, divided by the reference intensity, reveals a certain level of noise coming from the system (the RMS is $\sim 4mV$). Occasionally, we observed some fluctuations in the waveform of the divided output signal like the one in Fig. **9**. These observations can be described by a certain amount of polarization fluctuations coming from the laser source. The producer guarantees a polarization ratio of 500:1: this ratio is probably reduced due to the wear and tear of the device. Since dividing the signal by the reference value we eliminate the intensity fluctuations, the remaining fluctuations are due to the polarization of the laser beam. Indeed, a fluctuation in the polarization is reflected in intensity fluctuations by the action of the polarizer placed in front of the crystal. A simple way to overcome this issue is to fix the initial polarization by inserting a polarizer in front of the laser source.

V. OPTICAL LINE DESIGN, FABRICATION AND TESTING

Now that we have determined the properties of the laser beam we can move on to the design of the optical line. This section will describe the building process of the optical line, the optical elements needed to reproduce the Sénarmont method, and the tests performed to set correctly those elements. The complete scheme of the apparatus is shown in Fig. **10**.

The Sénarmont method (Sec. **I.2**) requires an initial polarized beam at $45°$ with respect to the vertical axis (y) in which the electric field is applied: for this reason we have inserted a polarizer (Pol2) before the sample. Then, after the crystal, we positioned a $\lambda/4$ waveplate with fast axis oriented at $45°$ with respect to the y-axis which linearly polarizes the outgoing beam. Finally, the beam is directed to the photodiode after passing another polarizer, called analyzer. All the optical components must be properly positioned with a procedure described in the following paragraphs. We started by finding the angular position for which the analyzer is orthogonal to the polarizer Pol2 (Sec. **V.1**). Therefore, by introducing the crystal, which fixes the reference of the vertical y-axis, it was possible to suitably rotate both the polarizer and the analyzer in order to correctly set them in the desired angular position (Sec. **V.2**). Similarly, after mounting the polarization optics, we set the $\lambda/4$ waveplate in its final configuration (Sec. **V.3**). We have also introduced an iris before the photodiode to remove the multiple reflections induced by the optical elements.

There are two important factors that need to be considered in the design of the optical line, which are the fluctuations both in intensity and in polarization of the laser source. To overcome the first problem we split the beam with a 50:50 beam splitter. One of the two outgoing beams is directed to a reference photodiode (PD_{ref}), while the other passes through the Sénarmont apparatus and is detected by the signal photodiode (PD_{sig}), which is used to measure the variations of the intensity induced by the birefringent crystal. In this way, the ratio between the signals recorded by PD_{sig} and PD_{ref} is independent by the intensity fluctuations of the laser source. More details about this procedure can be found in Sec. **VI** where we discuss the dividing electronic system.
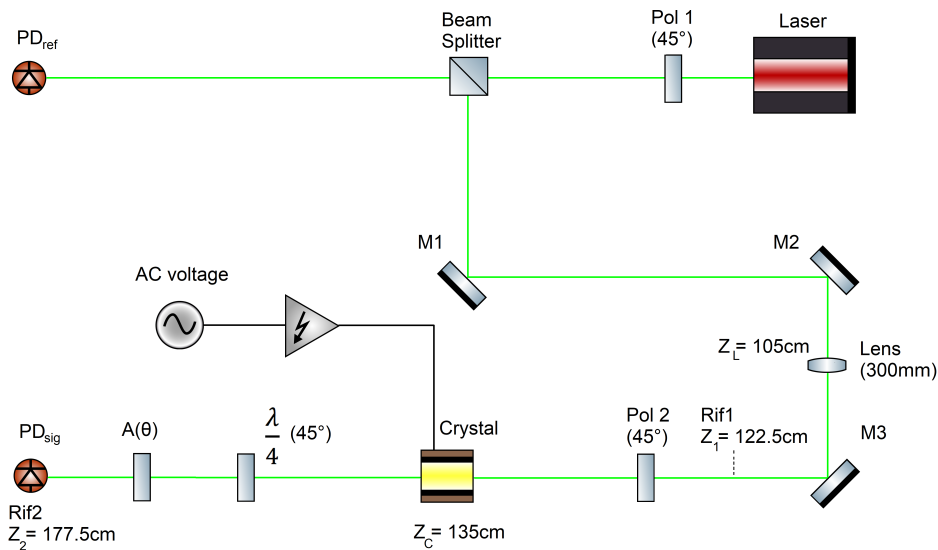

FIG. 10. Schematic of the optical line.

The second factor to take into account consists in the polarization fluctuations of the laser beam. This phenomenon affects the intensity measurements carried out with the photodiode PD_{sig} (see Sec. **IV.3**). If the polarization of the laser beam changes, so does the intensity of the beam after the polarizer Pol2, according to Malus' law. This problem can be easily solved by introducing a polarizer (Pol1) before the beam splitter which fixes the polarization of the incoming beam. We set the polarizer Pol1 to be parallel to Pol2 in order to maximize the measurable intensity with PD_{sig}. Other adjustments have become necessary to improve the performance of the apparatus. We have introduced a set of three mirrors (M1, M2, M3): this procedure is crucial not only to gain space in the optical bench but also because in this way the height and the direction of the beam can be finely adjusted. At this point we defined two reference positions (Rif1 and Rif2) for the measurement of the beam waist through the CCD (Rif2 coincides with the position of PD_{sig}). The position in the optical path corresponding to Rif1 is $z_1 = 122.5cm$ while for Rif2 is $z_2 = 177.5cm$. The measured beam waists are: $W(z_1) \sim 0.69mm$ and $W(z_2) \sim 0.89mm$. We want a beam waist small enough, compared to the sample thickness (which is $4mm$) to avoid clipping: the beam waist should be smaller than $1/6$ of the sample thickness. We introduced a biconvex lens with a focal length 300 mm at the position $z_L \sim 105cm$ to focus the beam. After the lens, the beam has a minimum waist $w_0' = 92\mu m$ at the position $z' = 139.5cm$ and the corresponding Rayleigh range is $z_R' = 49.3mm$. For practical reasons we inserted the crystal at a position $z_C \sim 135cm$: in this way the beam waist inside the sample is $W(z_C) \sim 150\mu m$, and at the position of the photodiode PD_{sig} it is $W(z_2) \sim 0.64mm$. With this configuration, the beam is completely contained within both the sample and the active section of the detector.

1. Polarizers orthogonality

The orthogonality of the polarizers is a condition required to properly set up the elements in the optical line. After defining the direction of propagation of the beam and inserting the focusing lens, the polarization optics can be adjusted. We started by inserting the polarizer Pol2 and the analyzer. We fixed the angle of the polarizer Pol2 at $\theta_P = 0°$. The angle of the analyzer was varied until a complete extinction of the light intensity measured with the photodiode was observed. To improve the estimation of this angular position we performed a fit of the measured intensities as a function of the angular position of the analyzer θ using a sinusoidal function (in agreement with Malus' law) of the following type: $I(\theta) = A sin(\omega\theta + \phi) + V_0$ (see Fig. **11**). From the results of the fit we have determined the relative angle between the polarizer and the analyzer so that they are orthogonal to each other. This angle is $\theta_A^\perp = (192.65 \pm 0.07)°$.

FIG. 11. Plot of the intensity measured with the photodiode as a function of the analyzer angle keeping fix the angle of the polarizer Pol2 at 0°. The angle which minimizes the intensity is $\theta_A^\perp = (192.65 \pm 0.07)°$.

2. Sample alignment

It is important to underline that the previous procedure allows to find the orthogonality condition between analyzer and polarizer but does not return information about their orientation with respect the vertical axis. The vertical reference direction (y-axis) is determined by the crystal reference frame. The refractive indexes of the crystal along the two orthogonal directions (x and y), when the electric field is turned off, are in principle equal: this means that the crystal does not change the polarization state of a beam propagating along the z-axis. If the crystal axis (z) is not parallel to the beam axis, a small residual birefringence is still present. This effect is observed experimentally by measuring the light intensity with the photodiode while simultaneously rotating both the polarizer and the analyzer so that they remain orthogonal. In principle, when the crystal axis is correctly aligned, the outgoing beam is still linearly polarized (with the same polarization of the incoming beam) and the analyzer should completely extinguish the beam intensity. If the crystal is not correctly aligned, it is possible to observe a variable intensity that depends on the polarization of the incident beam. Two micrometric screws allow fine adjustments of the direction of the crystal in order to properly align its axis to the beam line.
Once aligned the crystal, we need to align the polarizer Pol2 to 45° with respect to the y-axis of the sample. The vertical y-axis is given by the direction of the applied electric field which induces the birefringence of
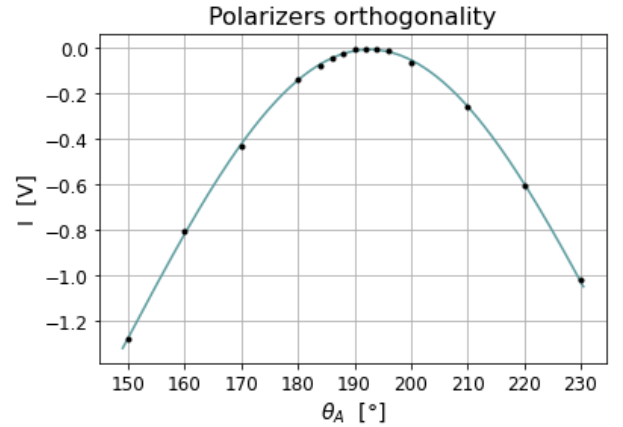
the crystal by changing the refractive indexes along the x and y directions (Eq. 7). To locate the y (or x) axis, consider that when an electric field is applied to the crystal and the incident beam is polarized along the x or y-axis, the outgoing beam preserves its original polarization and we observe a complete intensity extinction. Otherwise, if the incident beam is linearly polarized in a different direction, the outgoing beam is elliptically polarized and the analyzer cannot completely extinct the intensity measured with the photodiode. This consideration can be applied to align the polarization of the incident beam to one of the two orthogonal axes. For this scope we applied a static electric field by setting a DC voltage of $500V$ and we rotated both the polarizer and the analyzer synchronously (keeping them orthogonal) until the observed intensity was minimized.

The results in Fig. 12 are fitted using a second-order polynomial function: $I(\theta) = a\theta^2 + b\theta + c$. The angle of the polarizer which minimizes the intensity is $\theta_P^{(0)} = (-9.85 \pm 0.08)°$.

The minimum intensity measured with the photodiode is $\sim -80mV$ while the background is $\sim -20mV$. We tried many times the procedure of alignment of the crystal and scan of the polarizers angle but we always found a small amount of residual birefringence: we have to consider that the assumption made in Eq. 7 of neglecting the off-diagonal terms is just an approximation. Since in the following analysis we will apply voltages in the range of $[0,20]$V we expect that the residual birefringence becomes negligible. After fixing the polarizer angle such that it polarizes the beam parallel to one of the two axes (x or y), we rotate both polarizer and analizer of $45°$ in their final configurations. From this analysis we don't know if the polarizer was aligned with the x or y-axis of the crystal but it is not important since, in any case, after the rotation, we have a polarization of the incident beam at $\pm45°$ with respect to the vertical axis. The Sénarmont method is valid in both situations. From now on we will conventionally define the polarization of the incident beam at $+45°$.

FIG. 12. Intensity measured by PD_{sig} as a function of the angular position of the polarizer Pol2. The angle which minimize the intensity is $\theta_P^{(0)} = (-9.85 \pm 0.08)°$.

3. Quarter waveplate alignment

The final step consists in the alignment of the $\lambda/4$ waveplate at $45°$. When the $\lambda/4$ waveplate is properly aligned, it doesn't change the polarization of an incident linearly polarized beam at $45°$ and it is possible to completely extinct the intensity of the outgoing beam by setting the analyzer to the orthogonal direction. We remove the crystal during the execution of this procedure, to avoid the effect of the residual birefringence. Since the polarizer axis is oriented at $45°$ and the analyzer is aligned in the orthogonal configuration, when the $\lambda/4$ waveplate fast axis is parallel to the first polarizer the intensity measured with the photodiode is minimized. In this way we get a first estimation of the optimal angle θ_{QWP}. In order to better estimate the optimal configuration we evaluated the visibility for different angles around θ_{QWP}. This quantity is defined as:

$$V = \frac{I_{max} - I_{min}}{I_{max} + I_{min}}$$

FIG. 13. Visibility obtained by varying the angular position of the $\lambda/4$ waveplate. The angle which minimize the visibility is $\theta_{\lambda/4} = (120.54 \pm 0.05)°$.

where I_{max} and I_{min} are respectively the maximum and minimum intensities measured with the photodiode through an analyzer scan. The best configuration of the waveplate corresponds to the maximum contrast between the minimum (ideally zero) and maximum intensity. The results in Fig. 13, fitted with a second-order polynomial function, show a maximum in the visibility at $\theta_{QWP} = (120.54 \pm 0.05)°$. Also in this case, we said that the waveplate fast axis is
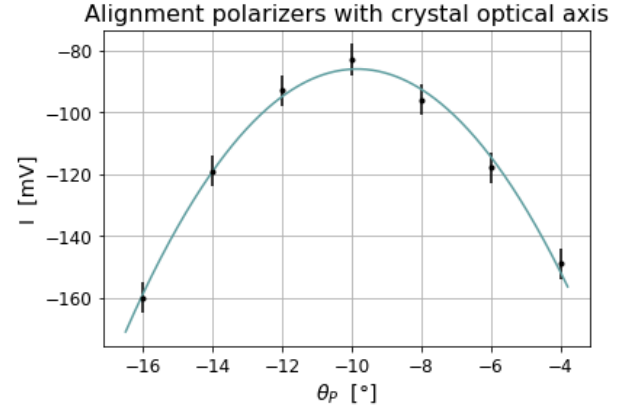
oriented at 45°; however this method does not allow to distinguish the configurations at ±45° since in both cases the waveplate doesn't change the polarization of the state. As in the previous case, it does not affect the Sénarmont method. After the waveplate alignment procedure, we reintroduced the crystal. Finally, the polarizer Pol1 was rotated in order to maximise the intensity recorded by PD_{sig}. All the optical elements have been positioned in their final configuration which is shown in Fig. **10**.

VI. ELECTRONIC DESIGN FOR DATA ACQUISITION

Once the entire optical line has been built and tested, it is possible to design the complete electronic chain for data acquisition. We need an apparatus capable of converting the photocurrents emitted by the two photodiodes into voltage signals (V_{sig} and V_{ref}) with a suitable conversion factor. It is also necessary to insert a divider module in order to divide electronically V_{sig} by V_{ref} and get the normalized output voltage V_{out} which is independent of the laser intensity fluctuations. For this scope we used the analog multiplier **AD633JN** (datasheet) with a proper feedback loop. The transfer function of the divider module is:

$$V_{out} = (-10V) \cdot \frac{V_{sig}}{V_{out}} \tag{31}$$

We started by measuring with the power meter the light power incident on both photodiodes: this procedure was carried out after completing the optical line in order to be able to accurately estimate the light power measured by each detector in the final configuration. Knowing the responsivity of the photodiodes PD_{sig}, PD_{ref} (Eq. **23**) we estimated the corresponding photocurrents, denoted as i_{sig} and i_{ref} respectively. From these quantities we can evaluate the gain of each module needed to reach the desired output voltages. It is important to notice that V_{sig} must be lower than V_{ref} to avoid the saturation of the output voltage of the divider module: this is due to the amplification factor $-10V$ of the ratio between the two voltages in Eq. **31**, while the supply voltages of the divider module are ±12V.
Now we describe the choices made in the design of the two modules relative to the reference and signal photodiodes (the complete electronic scheme is presented in Fig. **14**).

- **Reference module:** The mean light power of the incident beam in PD_{ref} is $P_{ref} \sim 150\mu W$ which corresponds to an induced photocurrent $i_{ref} \sim 35\mu A$. We want to obtain an output signal $V_{ref} \sim 4V$ and so we need a circuit with a gain corresponding to $G_{ref} = \frac{V_{ref}}{i_{ref}} \sim 1.2 \cdot 10^5 V/A$. The initial stage consists in a transimpedance amplifier, which, as discussed in Sec. **II**, converts the photocurrent to a proportional voltage signal. This module is connected to an inverting amplifier. This choice is motivated by the fact that we need not only to amplify but also to invert the negative output voltage exiting from the transimpedance amplifier: the multiplier AD633JN, indeed, must receive positive signals at the denominator otherwise it saturates. Moreover, it is not convenient to use a single amplification module with high resistance, since it increases the noise of the output signal. A set of three resistors R_1, R_2, and R_3 has been used for this module (Fig. **14**). The total gain is given by:

$$G_{ref} = \frac{R_1 R_3}{R_2} = (1.23 \pm 0.03) \cdot 10^5 \frac{V}{A} \tag{32}$$

- **Signal module:** The mean light power of the beam incident in PD_{sig} is $P_{sig} \sim 25\mu W$ which corresponds to an induced photocurrent $i_{sig} \sim 5.8\mu A$. Since we want to obtain an output voltage $V_{sig} \sim -3V$ we need a gain $G_{sig} = \frac{V_{sig}}{i_{sig}} \sim -5.3 \cdot 10^5 V/A$ (the minus sign derives from the conventional choice of defining positive photocurrents). Also in this case the module has been divided into two stages: a transimpedance amplifier followed by a non-inverting amplifier, since in this case it is not necessary to invert the sign of the output voltage of the transimpedance amplifier. We introduced a set of three resistors R_4, R_5 and R_6 (see Fig. **14**). The gain of this module is given by:

$$G_{sig} = -R_4 \left(1 + \frac{R_6}{R_5} \right) = (-4.83 \pm 0.09) \cdot 10^5 \frac{V}{A} \tag{33}$$

These two modules have been connected to the divider (Fig. **14**) which, as discussed in the AD633JN datasheet, can be obtained by adding to the multiplier a suitable feedback loop.
After verifying the correct functioning of the entire apparatus we proceeded to solder the components to a circuit board

that can be connected to a module of the NIM CAEN N8315 crate. This procedure turned out to be fundamental for the electronic noise reduction, while at the same time, we observed greater stability in the apparatus. The following sections are dedicated to the characterization of the modules which is an important procedure for the final analysis that we will describe in Sec. **VII**.
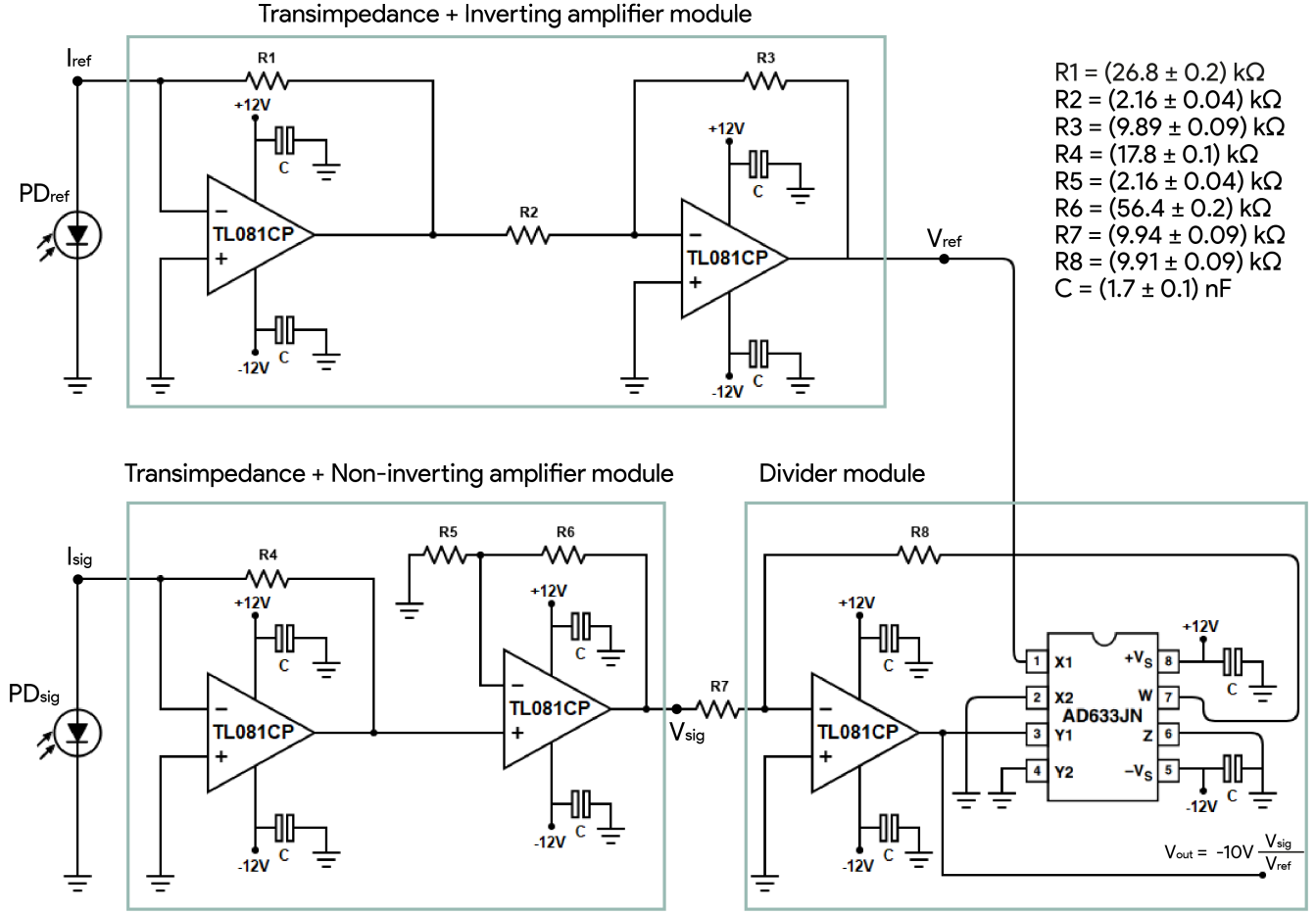

FIG. 14. Scheme of the complete electronic circuit.

### 1. Characterization of the photodiode linear response

We followed the same procedure discussed in Sec. **II** to characterize the linear response of the electronic modules connected to the two photodiodes: *transimpedance + inverting amplifier* (Reference) and *transimpedance + non-inverting amplifier* (Signal). The resistors employed for the realization of these modules together with the scheme of the electronic circuits are reported in Fig. **14**. We fit data with a function of the form $P(I) = mI + q$, where P is the power measured with the power meter and I is the intensity measured with the photodiode modules expressed in terms of their output voltages. The results are presented in Fig. **15b** and Tab. **1**. Note that m is the conversion factor from V to μW, while q is a shift that appears to be compatible with $0\mu W$ in both cases.

We demonstrated that the output voltages of each module are linearly dependent on the intensity of the incident radiation thus providing a good method to estimate the intensity of the beam passing through the photodiodes.

These modules are more complicated than the simple transimpedance amplifier described in Sec. **II**. As previously mentioned, the choice of introducing two amplifier modules, together with using smaller resistances, has allowed to achieve greater gains and less noise. The estimated RMS in both situations is $\sim 7mV$, which can be lowered to even less mV by forcing the oscilloscope to display mean signals.

	m [$\mu W/V$]	Pearson coefficient r
Reference	34.6 ± 0.2	0.99992
Signal	-17.9 ± 0.1	0.9998

TAB. 1: Conversion factor and linearity (Pearson coefficient) for both modules (Reference and Signal).
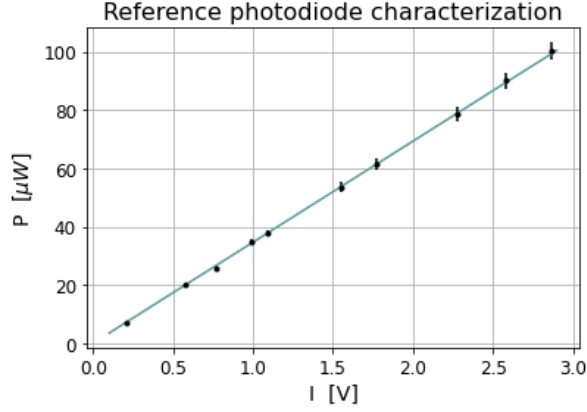
(a) Characterization of PD_{ref} electronic module
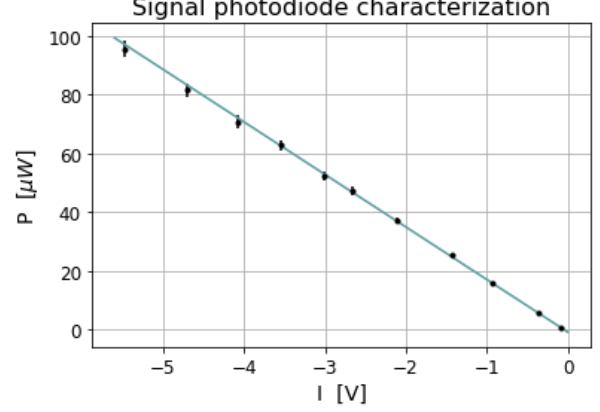
(b) Characterization of PD_{sig} electronic module

FIG. 15. Light power measured with the power meter as a function of the output voltages of the two modules: Reference (**15**a) and Signal (**15**b).

2. Frequency response of the electronic system

The experimental apparatus was devised to measure the electro-optic coefficient r_{22} by applying an AC voltage to the crystal. The corresponding intensity signal detected by PD_{sig}, which depends on the oscillating phase induced by the crystal, is itself an oscillating signal. Since the amplification gain of an amplifier depends on the frequency of the input signal we need a frequency characterization of the response of the electronic device.

The phase shift introduced by the crystal, which depends on r_{22}, could depend on the frequency of the applied electric field, therefore this procedure cannot be performed directly by varying the frequency of the voltage signal applied to the sample. For this scope, we simulated the photocurrent induced in PD_{sig} by directly applying an alternating current signal with the proper amplitude to the corresponding module. This current has been obtained by applying an alternating voltage signal with offset $V_{off} = 100mV$ and amplitude $V_{amp} = 10mV$ (produced by the AC generator)

FIG. 16. Frequency response of the divider circuit: the gain of the circuit, defined as the ratio $G = \frac{V_{out}}{V_{amp}}$, is plotted as a function of the AC frequency of the simulated signal.

to a resistor $R = 18k\Omega$. At the denominator of the divider module we used a constant signal of $4V$ to simulate the voltage coming from the reference electronic module. Then we measured the output voltage of the divider V_{out} for different frequencies of the input signal. The gain of the electronic circuit as a function of the frequency of the input signal is shown in Fig. **16**. The circuit behaves as a low-pass filter with a break frequency $f = (56.5 \pm 0.7)kHz$.
This study is crucial to define the frequency range in which it is possible to apply the analysis described in Sec. **VII**. In this sense, it defines the limits of our detection apparatus.
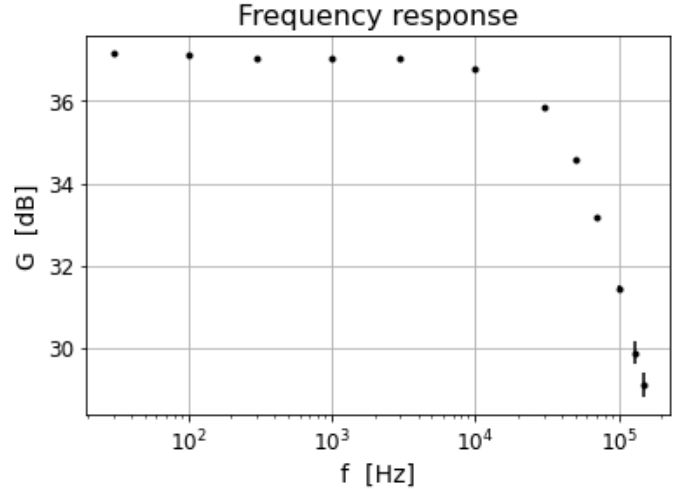
VII. ANALYSIS AND RESULTS

Given the work described in the previous chapters, we are now able to study the response of the Sénarmont apparatus as a function of the voltage signal applied to the crystal to estimate the r_{22} electro-optic coefficient. From now on we will consider the normalized value that comes from the divider circuit as the measure of the intensity I transmitted by the crystal. In agreement with Eq. 19, the transmitted intensity is:

$$I(\theta_A, \delta) = \frac{I_0}{2}[1 + \cos(2\theta_A + \delta)] + I_{bkg} \tag{34}$$

where δ is the phase delay introduced by the crystal due to the electro-optic effect, I_0 is the difference between the maximum and minimum intensity and we also included a background factor I_{bkg}.

To estimate the r_{22} coefficient we exploit a linearization of the cosine function in Eq. 34. As described in Sec. I.2, we first have to rotate the analyzer in order to reach the configuration that corresponds to half of the transmitted intensity $\left(I(\bar{\theta}_A, \delta = 0) = \frac{I_0}{2}\right)$. The condition $\delta = 0$ implies that no phase delay is applied to the incoming beam. We start with this case because we are interested in studying the response of the Sénarmont apparatus in the absence of an external electric field applied to the crystal. Once the appropriate angle $\bar{\theta}_A$ is selected, we can study the response of the system for small variations of the optimal angular position (θ_A), thus obtaining the linear coefficient mapping a variation in the analyzer angle to a variation in the measured intensity. However, the aim of this type of analysis is to map the measured intensity in the phase delay δ introduced by the crystal. This can be done considering that the slope of the linearization of $I(\theta_A, \delta)$ for small values of δ is half the slope estimated by varying θ_A. The analysis we described in Sec. I.2 naturally reflects this consideration (see Eq. 20 and 22).

This section is organized as follows: in Sec. VII.1 we will describe the procedure to find the desired angle $\bar{\theta}_A$ and the study of the linear response of the apparatus around this configuration. In Sec. VII.2 we will present the measures and estimations of the parameters needed to estimate the r_{22} coefficient, while in Sec. VII.3 we will describe the measurement process and the analysis method adopted. Finally, in Sec. VII.4 we will present and discuss the obtained results.

1. Characterization of the apparatus response in the linear regime

To estimate the optimal angular position of the analyzer $\bar{\theta}_A$, we collected the voltages produced by the electronic device by varying the analyzer angle in a range of 180 degrees with a null voltage applied to the crystal. We inserted an absorptive neutral density filter with an optical density 0.3 in front of PD_{sig}, which halves the measured intensity, due to the fact that the gain provided by the electronics is high enough to make the output of the circuit saturate. The experimental data were fitted with a sinusoidal function (Fig. 17a):
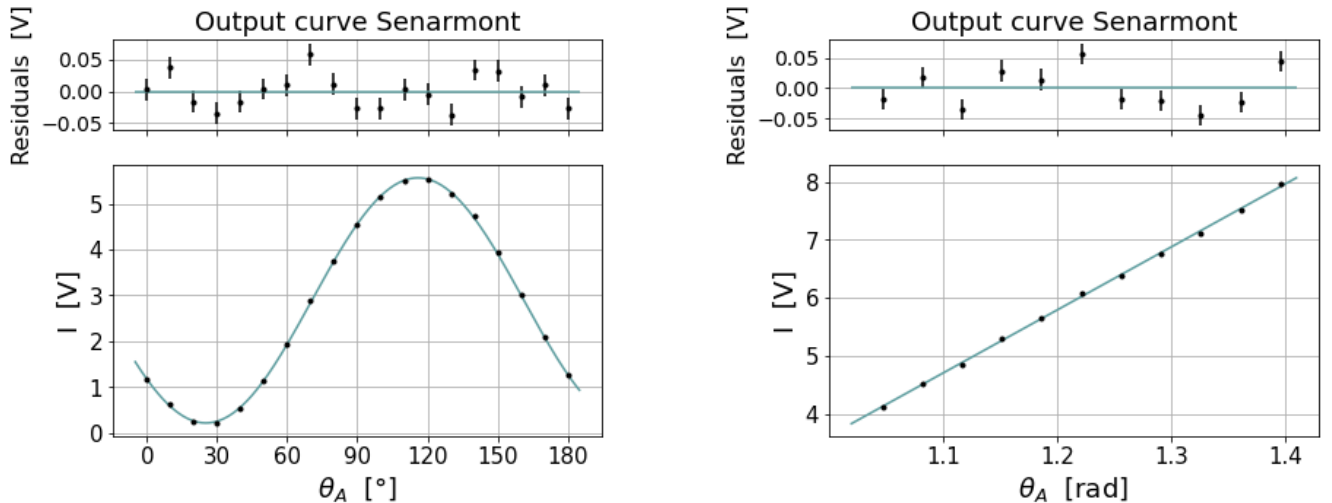
(a) Response curve of the analyzer. Please note that the displayed angle θ_A refers to the value read on the rotation mount of the polarizer. It differs from the analog angle cited in Eq. 34 by a constant shift. The intensities are halved due to the absorptive neutral density filter.

(b) Response curve in a linear approximation. Pearson coefficient $r = 0.9996$

FIG. 17

We fitted the collected data to estimate the angle $\bar{\theta}_A$ which allows to observe the response at half of the maximum intensity, obtaining:

$$\bar{\theta}_A = (70.6 \pm 0.1)° = (1.231 \pm 0.002) rad \tag{35}$$

Once the analyzer angle is set at this specific value, we are confident that, for voltages below a certain threshold applied to the crystal, the response of the system will be linear. Expanding Eq. 34 around $\bar{\theta}_A$ we get an approximated linear behavior with an uncertainty at most of $\sim 1\%$, which corresponds to a maximum phase shift of $\sim 14°$, if the intensity variation $\Delta I = I(\bar{\theta}_A, \delta) - \frac{I_0}{2}$ is lower than $\sim 2.3V$. In our case, since to perform the measures we will apply to the crystal a voltage smaller than 20V, the maximum variation of the intensity measured with the photodiode is $\sim 600mV$: this means that the maximum phase shift is $\sim 4°$ which corresponds to a maximum uncertainty of the linear approximation lower than 0.1% in the experimental results.

We studied the linear response of the system keeping a null voltage applied to the crystal and removing the neutral density filter previously inserted. Fig. 17b shows the data acquired in the laboratory in proximity to $\bar{\theta}_A$ and the corresponding linear fit. We estimated the linear coefficient k, which Eq. 22 shows to be equivalent to I_0, as:

$$k = (10.9 \pm 0.1)V \tag{36}$$

This parameter plays a key role in the estimation of the electro-optic coefficient r_{22} of the crystal since it allows to map the measured intensities to the corresponding phase shift induced by the sample birefringence.

2. Parameters for r_{22} estimation

Eq. 21 will allow us to estimate the r_{22} electro-optic coefficient of the crystal. While we already know from the laser specifications that the wavelength of the optical beam is $\lambda = 543.5nm$, we need to measure the parameters L, d, which are the dimensions of the crystal along the z-axis and the y-axis respectively (the latter is equal to the dimension along the x-axis, since the crystal has the geometrical shape of a parallelepiped with a square base). We measured such dimensions by means of a caliper:

$$L = (23.80 \pm 0.01)mm \qquad\qquad d = (4.36 \pm 0.01)mm$$

The estimation of the ordinary refractive index n_o can be conducted by exploiting the empirical Sellmeier relations, as described by Bartnick et al. [4] for the wavelength $\lambda = 543.5nm$. We can estimate the parameter n_o through Eq. 37, which leads to the following plot:

$A_1 = 4.9048$

$A_2 = 0.11775\mu m^2$

$A_3 = 0.21802\mu m$

$A_4 = 0.027153\mu m^{-2}$

$B_1 = 2.2314 \cdot 10^{-8}\mu m^2/°C^2$

$B_2 = -2.9671 \cdot 10^{-8}\mu m/°C^2$

$B_3 = 2.1429 \cdot 10^{-8}°C^{-2}$

$C_1 = 24.5°C$

$C_2 = 570.5°C$

TAB. 2: Sellmeier coefficients.

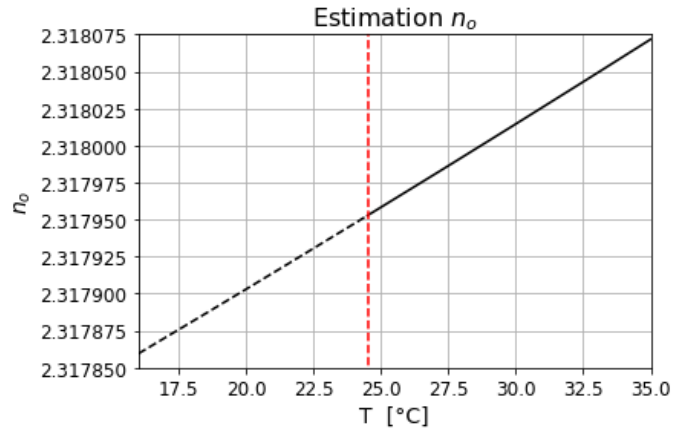**FIG. 18.** Estimated behavior of the ordinary refractive index of $NbLiO_3$ for temperatures within the range $[24.5°C, 35°C]$. The black dotted line is the estimated behavior for lower temperatures.

$$n_o(\lambda[\mu m], T[K]) = \sqrt{A_1 + \frac{A_2 + B_1(T - C_1)(T + C_2)}{\lambda^2 - [A_3 + B_2(T - C_1)(T + C_2)]^2} + B_3(T - C_1)(T + C_2) - A_4\lambda^2} \tag{37}$$

To be precise, the Eq. 37 has been proven to be valid by Bartnick et al. [4] for temperatures higher than $24.5°C$, while in the laboratory we had temperatures in the range $[17°C, 22°C]$. However, since there are small variations of the n_o value for the range covered by Fig. 18, we are confident that we can exploit the empirical equation above to estimate n_o also in the temperature range of the laboratory. We estimated this quantity as the mean value for $T \in [17°C, 22°C]$:

$$n_o = 2.31790 \pm 0.00003 \tag{38}$$

3. Data acquisition and analysis method

We are now able to exploit the Sénarmont apparatus to acquire the data necessary for the estimation of the coefficient r_{22}. First, we decided to estimate the electro-optic coefficient for different frequencies of the sinusoid voltage signal applied to the crystal. Referring to Fig. 16 we note that, due to the high circuit gain, which allows high resolution in voltage measures, we have a restricted range of frequencies in which the signals are not clipped. For this analysis we selected 5 frequencies: 0Hz, 100Hz, 1kHz, 5kHz, and 10kHz. We used a high voltage generator (HVG) present in the laboratory to generate DC signals, while AC signals are generated by the AFG-2225 (datasheet) AC voltage generator.

Once the analyzer angle is set according to the estimation in Eq. 35 and the frequency of the voltage signal connected to the crystal has been set, the data acquisition process consists in varying the amplitude of this signal in a range of $[0,20]\ V_{pp}$ (the subscript pp denotes that it is a peak-to-peak voltage) and observing the sinusoidal signal recorded by the oscilloscope connected to the electronic device. We have saved all the waveforms recorded with the oscilloscope in different files to exploit an offline analysis. All the waveforms have been recorded using the AC mode of the oscilloscope (apart from the ones regarding the measurement at $f = 0Hz$), thus discarding the DC voltage underlying the waveform. Regarding the waveform recorded with the oscilloscope, we are mainly interested in its amplitude, since from the estimation of k (Eq. 36) we are able to map the signal amplitude to the corresponding phase shift introduced by the crystal. To estimate the amplitude of each waveform, we exploited a sinusoidal fit on the waveform recorded with the oscilloscope. The following graphs show two examples of the analysis carried out on the data obtained by applying a sinusoidal voltage to the crystal with frequency $f = 100Hz$ and amplitudes $3V_{pp}$ and $9V_{pp}$, respectively.

(a) Estimated amplitude: $A = (48.32 \pm 0.05)mV$.   **(b)** Estimated amplitude: $A = (152.82 \pm 0.05)mV$.
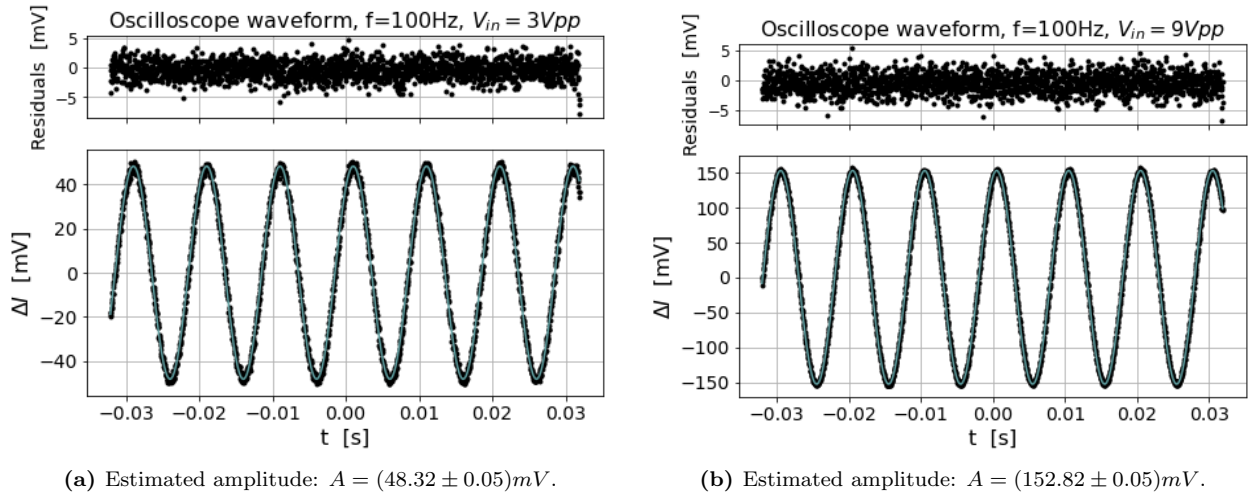
FIG. 19. Example of the analysis performed to obtain the amplitude of the output signal. The waveforms have been recorded using the AC mode of the oscilloscope.

We have to note that this type of analysis produces very low uncertainties in the measured amplitudes, which are on the order of $10^{-2}mV$ for most of our datasets. These uncertainties seem to be highly underestimated with respect to the real ones. On the other hand, looking at the residual plots in the previous figures, we notice that the noise underlying the measurement is quantified in a few millivolts. Indeed, the posterior error for different waveform datasets is generally close to $2mV$. This value is compatible with the RMS of the output signal of the electronic device we have designed. We also noted that a little uncertainty in the amplitudes arises from the position of the

trigger. From these considerations, we believe that any kind of amplitude estimation cannot be performed with an uncertainty smaller than $2mV$. We thus proceed to assign an uncertainty of $2mV$ to all the amplitudes estimated by the fit. This uncertainty is good enough to describe the distribution of the experimental data in Fig. **20** and in the appendix section **IX.2**.

The considerations and the analysis method discussed above hold when working with frequency signals. Instead, for data taken in the DC regime, we simply estimated the output of the apparatus as the average value recorded by the oscilloscope, using the observed RMS as its uncertainty. We observed that generally the RMS obtained working in the DC regime of the oscilloscope ($RMS_{DC} \sim 7mV$) is quite higher than the same quantity evaluated in the AC regime ($RMS_{AC} \sim 2mV$). For this reason, the data measured in the DC regime are affected by a greater uncertainty (Fig. **23**).

Combining Eq. 21 and 22 with the estimation of the linear coefficient k (Eq. 36) we can rewrite:

$$\Delta I = k \frac{\pi}{\lambda} \frac{Ln_o^3 r_{22}}{d} \cdot V_{pp,cry} = m \cdot V_{pp,cry} \tag{39}$$

where $k = I_0$, $m = k \frac{\pi}{\lambda} \frac{Ln_o^3 r_{22}}{d}$, $V_{pp,cry}$ is the peak-to-peak voltage applied to the crystal and $\Delta I = 2A$ with A being the estimated amplitudes of the output signals described above.

The first step for the measure of the electro-optic coefficient r_{22} consists in estimating the linear coefficient m. This is done by performing a linear fit of the data $(x, y) = (V_{pp,cry}, \Delta I)$. Here, we present as an example the plot of the observed intensity as a function of the peak-to-peak voltage applied to the crystal at the frequency $f = 100Hz$, while the remaining plots are collected in the appendix (Sec. **IX.2**). The m coefficients estimated at different frequencies are collected in Tab. **3**.
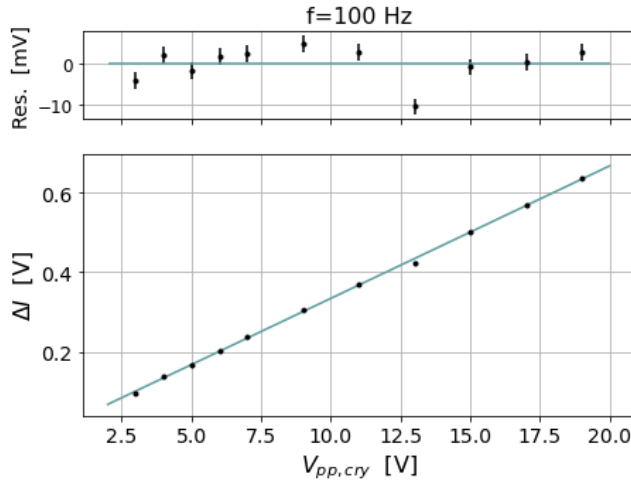
f [kHz]	m [$\cdot 10^{-4}$]
0	342 ± 3
0.1	333 ± 3
1	333.6 ± 0.8
5	333 ± 2
10	330 ± 1

FIG. 20. Observed intensity as a function of the peak-to-peak voltage applied to the crystal in the linear regime at $f = 100Hz$.

TAB. 3: Values of m estimated at different frequencies.

4. Results

Once estimated the linear coefficient m, from Eq. 39 it is possible to estimate r_{22} as:

$$r_{22} = \frac{\lambda d}{\pi Ln_o^3} \frac{m}{k} \tag{40}$$

The estimations of the electro-optic coefficient at different frequencies are summarized in Fig. **21** and Tab. **4**.

An observation we deduce from the plot in Fig. **21** is that the estimation in the DC regime appears to be biased with respect to the other values. From the literature [5], we expect a constant r_{22} at low frequencies, so this fact is probably due to experimental reasons. In the appendix (Sec. **IX.1**) we studied the transfer function of the crystal by modeling it as a resistance in parallel with a capacitance. Our aim was to study its behavior when connected to the AC voltage generator to investigate whether it could play a role in biasing the DC estimation of r_{22}. What we
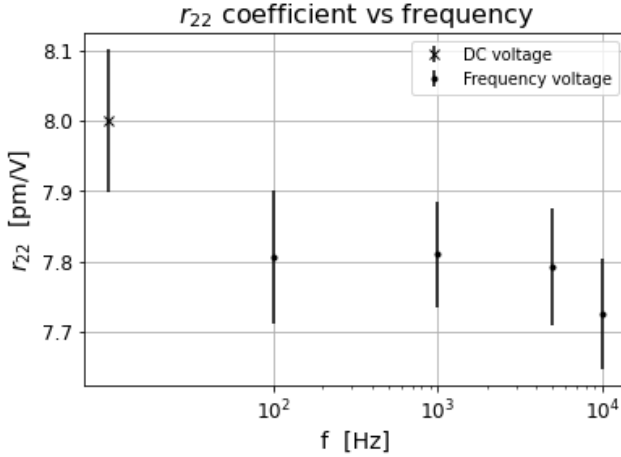
FIG. 21. r_{22} estimations at different frequencies.

f $[kHz]$	r_{22} $[pm/V]$
0	8.0 ± 0.1
0.1	7.81 ± 0.09
1	7.81 ± 0.08
5	7.79 ± 0.08
10	7.73 ± 0.08

TAB. 4: Values of r_{22} estimated at different frequencies.

found out is that the crystal behaves like a low-pass filter, with a break frequency much higher than the ones we are interested in, so it cannot explain this kind of result.

A possible explanation of the biased estimation in DC is obtained considering that we used the HVG to generate the DC signal applied to the crystal, while to generate the AC signal we relied on the AC voltage generator. Typically, these generators are affected by a scaling error: the signal that is actually produced is proportional to the indicated by the instrument and depends on the scaling factor, which is 1 in the ideal case. It should be noted that this effect alters the values of the effective voltage signals applied to the crystal with a proportional factor that does not modify the linear trend of the results, but affects the linear coefficient m. Since we used two different generators for the measurements in DC and AC, we expect two different scale factors and, as a consequence, two different systematic errors in the estimations of the r_{22} coefficient. Regarding the AC measures, we find that the systematic error is approximately 1% of the r_{22} estimation, so it does not significantly increase the uncertainties declared in Tab. 4. On the other hand, we do not have a datasheet regarding the HVG, but we can hypothesize that it has a different scale factor, thus explaining the bias of the DC measurement.

Another result that seems to show a small bias, as can be seen in Fig. 21, is the one obtained at $f = 10kHz$. Besides the good compatibility with the other AC estimations ($c \sim 0.6$), we suspect that this value does not depend on the statistical fluctuations of the performed measurements. Analyzing the plot in Fig. 16, we note that at $f = 10kHz$ the signals start to be clipped by the electronic transfer function. Since a reduction in signal amplitude produces a smaller coefficient m, we get a smaller coefficient r_{22}. It can be deduced that the bias in the estimation at $f = 10kHz$ is mainly caused by the cut introduced by the response function of the electronic setup we used.

Apart from the r_{22} estimations at $f = 0Hz$ and $f = 10kHz$, the remaining ones are all close to each other and perfectly compatible. We can exploit these three values to produce a final estimation of the r_{22} electro-optic coefficient at low frequencies, obtained by evaluating their mean:

$$\bar{r}_{22} = (7.803 \pm 0.004)\frac{pm}{V}$$

In many articles ([5], [6], [7]) the estimated electro-optic coefficient r_{22} for a pure $LiNbO_3$ crystal is $r_{22} = 6.8pm/V$. Our estimate is $\sim 15\%$ higher than the corresponding literature value. This fact may be due to the effect of impurities inside the crystal ([6], [7]) or to systematic errors introduced by the experimental apparatus. This last point, in particular, takes into account the effect of the misalignments of the polarization components (as discussed in [8], [9]) but also of the imperfect alignment of the optical axis of the crystal. In particular, the latter is one of the most delicate points of the experiment. Small variations in the direction of the optical axis with respect to the beam axis induce a variation of the birefringence effect with a consequent bias on the final estimation of r_{22}. Despite these systematic uncertainties, mainly due to the limit of the experimental setup, our final estimate is quite precise and provides a small statistical uncertainty that confirms the effectiveness of the Sénarmont method for measuring the birefringence induced by an anisotropic crystal.

VIII. CONCLUSIONS AND FUTURE PERSPECTIVES

In this work we have described the experimental procedure to estimate the r_{22} electro-optic coefficient of the $LiNbO_3$ crystal through the Sénarmont method. In particular, we focused on the experimental methodology and approach, with particular regard to the choices made to overcome some problems encountered during the experiment.

We started with the description of the photodiode, the transimpedance amplifier, and the corresponding characterization, which becomes necessary in order to correctly quantify the intensity of the beam. Then we proceeded to the calibration of the CMOS sensor employed to characterize the laser beam. This procedure, together with an analysis of the laser instability, allowed us to design the setup of an optical line capable of splitting the optical beam, whose polarization is fixed by a polarizer. One branch of the optical line is directed to the crystal (producing the signal), while the other one is used as a reference for the intensity. We proceeded with a description of the procedure employed for the positioning of the optical elements in their working configuration. Finally, after completing the optical setup, we designed, built, and characterized an electronic system capable of amplifying the electrical signals coming from both photodiodes and dividing them: this normalization procedure allowed us to reduce the uncertainty on the final measurements by removing the intensity fluctuations due to the unstable laser source.

The analysis of the electro-optic coefficient r_{22} was carried out by applying an AC electric field to the crystal. This choice was motivated by the physical interest of evaluating the variation of this coefficient at different frequencies, as described in many articles (for example, [10], [5]), which is an important feature for many practical applications, such as optical modulators. In addition, this type of approach allows to better filter the electronic noise of a signal with a known frequency (this could have been done, for instance, by means of a phase-sensitive detector).

One of the most important points to consider in an electronic system that works with AC signals is the bandwidth, which defines the frequency range within which we can carry out the measurements. In our case, we needed to amplify small current signals, so we built an electronic device with high amplification factors. As a consequence, we obtained a circuit with a bandwidth of $\sim 60kHz$, while the range of frequencies for which the gain is approximately constant is [0Hz,10kHz]. A possible solution to increase the bandwidth of the electronic device consists in introducing a higher number of intermediate amplifier modules in order to reduce the gain of each amplifier. However, the resulting increase in electronic noise must also be considered. Another improvement consists in introducing a high-pass filter after the transimpedance amplifier related to PD_{sig}. In this way, we can directly amplify the AC signal and remove the DC component ab initio. This solution, together with the previous one, would allow us to further increase the AC signal amplification factor, improving the accuracy of the measurements. On the other hand, the DC component is used to define the optimal configuration of the analyzer (corresponding to half of the maximum intensity) and to define the coefficient of proportionality between the variation in intensity and the corresponding phase shift. In this case, an additional module should be added to separate the DC component from the AC one so that both signals can be treated separately.

We verified that until 10kHz the electro-optic coefficient is approximately constant: the estimated value is $r_{22} = (7.803 \pm 0.004)pm/V$. The results reflect the same behavior at low frequencies that can be found in the literature [5], even if our estimation is slightly higher than the expected one. We discussed the possible systematic errors introduced by the experimental setup. Among the various possible contributions, we believe that one of the most significant is due to a small inclination of the optical axis of the crystal with respect to the beam axis. Beyond these criticalities, which strongly depend on the quality of the experimental setup, the Sénarmont method is an efficient and robust way to estimate the electro-optic coefficients. There are other techniques for measuring them, based for example on interferometric measurements, which have the advantage of completely determining the dielectric tensor but are very sensitive to external influences. For this reason, the Sénarmont method remains the most used approach in the literature to accurately estimate the electro-optic coefficients of many crystals.

IX. APPENDIX

1. Crystal transfer function

The crystal is placed between two metal foils that act as a capacitor. Now we describe a simple model of the crystal in order to predict its behavior under the action of an oscillating electric field (see Fig. **22**a). The capacitance formed by two plates closely spaced to each other can be estimated as $C = \epsilon_0 \epsilon_r \frac{S}{d}$, where $\epsilon_0 = 8.854 \cdot 10^{-12} F/m$ is the vacuum dielectric constant, $S \sim 96mm^2$ is the surface of the two capacitor plates and $d \sim 4mm$ is their distance. The dielectric permittivity of the $LiNbO_3$ along a direction orthogonal to the optical axis at low frequencies is $\epsilon_r \sim 44$ [11]. We also need to consider the effect of the crystal's resistance, which can be modeled as a resistor in parallel to the capacitor. This can be done by considering the resistivity of the crystal at the environmental temperature, which is $\rho \sim 10^{10} \Omega \cdot cm$ [12].

We obtain the following estimations for the parasitic capacitance and resistance of the crystal:

$$C \sim 9.3pF \qquad\qquad\qquad R = \rho \frac{d}{S} \sim 4.1 \cdot 10^9 \Omega \qquad\qquad (41)$$

Fig. **22**a shows the model we introduced to describe the crystal. We inserted a parasitic resistance before the crystal, approximately equal to the output resistance of the voltage generator. This quantity is declared to be $r = 50\Omega$.

The circuit response (T) as a function of the angular frequency of the AC generator (ω) is given by the following formula:

$$T(\omega) = \frac{V_{AB}}{V_{in}} = \frac{1}{(1 + \frac{r}{R}) + j\omega rC} \qquad \Rightarrow \qquad |T(\omega)| = \frac{1}{\sqrt{(1 + \frac{r}{R})^2 + (\omega rC)^2}} \qquad (42)$$

where $j = \sqrt{-1}$ is the imaginary unit. The break frequency is $f_0 = \omega_0/2\pi$, where ω_0 is defined as follows:

$$|T(\omega_0)| = \frac{|T_{max}|}{\sqrt{2}} \qquad \Rightarrow \qquad \omega_0 = \frac{\sqrt{2 - (1 + \frac{r}{R})^2}}{rC} \sim \frac{1}{rC} \qquad \Rightarrow \qquad f_0 \sim 340MHz \qquad (43)$$
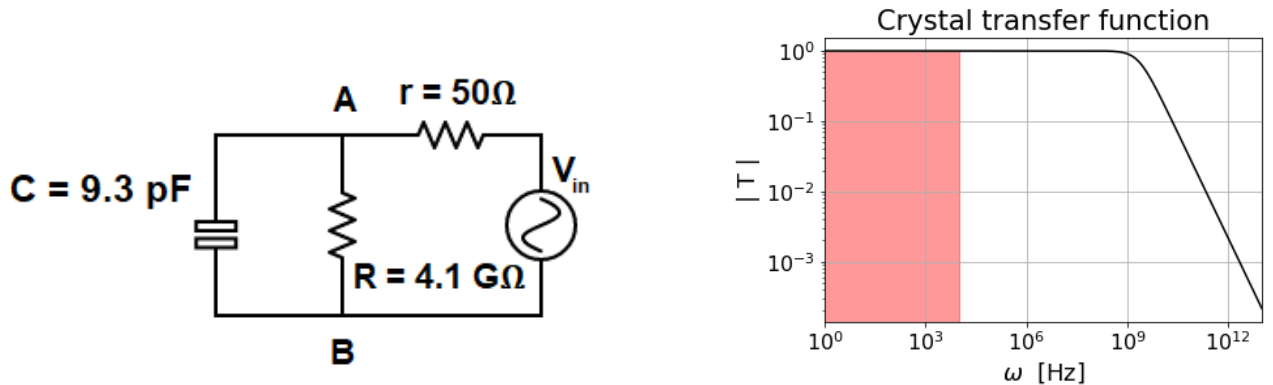
(a) Schematic of the circuit. The crystal introduces both a capacitance C and a resistance R (connected in series). The parasitic resistance introduced by the generator is represented by r.

(b) Crystal response function T. The red band highlights the frequency region in which we performed our measurements.

FIG. 22

The effect of the crystal resistance appears to be negligible due to its high value, and the overall effect of the crystal can be approximated as a low-pass filter with a large bandwidth. Since the break frequency is much larger than the frequencies employed in this experiment, we can neglect the distortion of the signal introduced by the crystal.

2. Linear fits for the estimation of r_{22} at different frequencies

We report here the remaining plots from which we estimated the m coefficients. The corresponding frequencies are: 0Hz, 1kHz, 5kHz, and 10kHz.
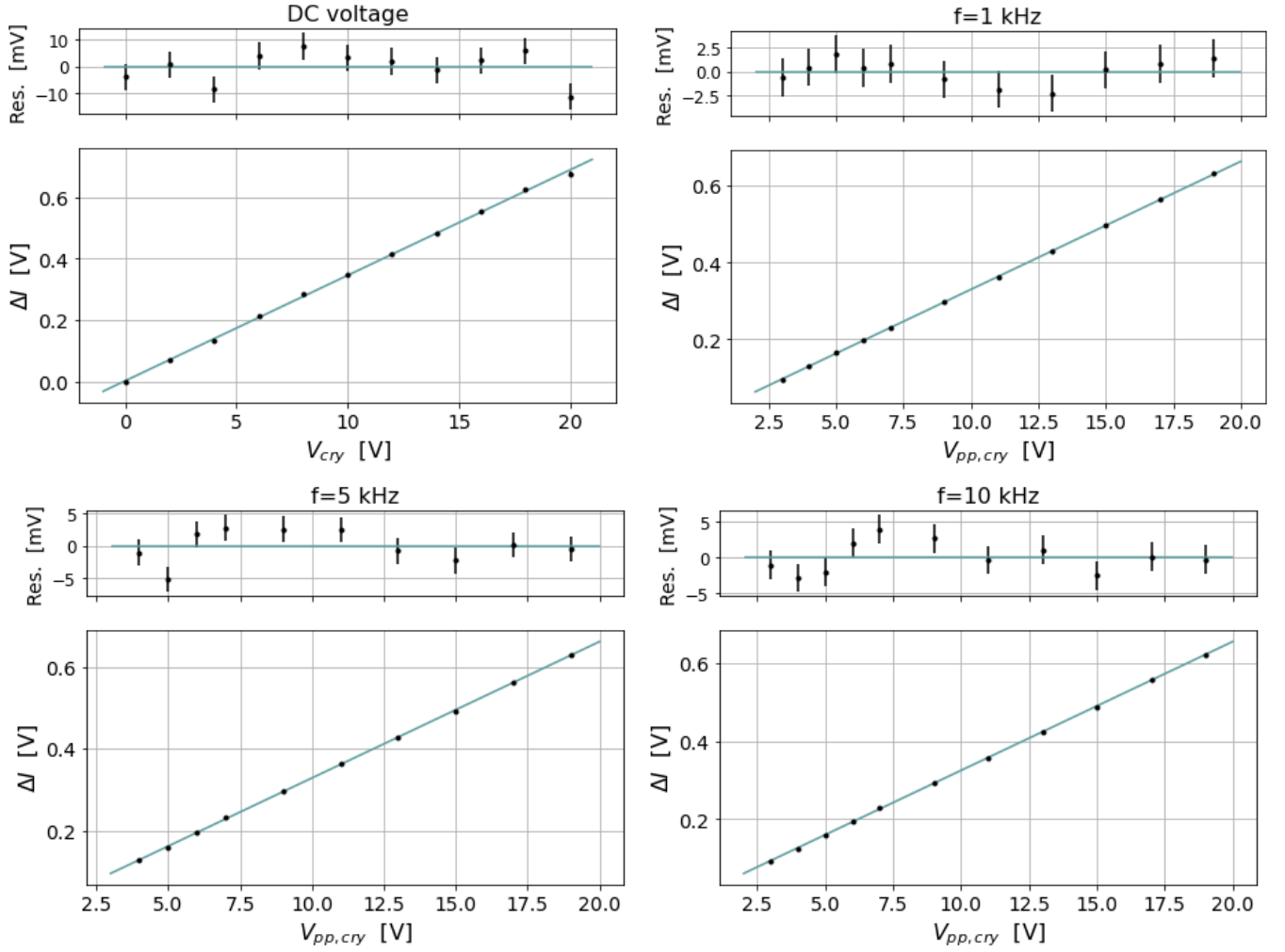

FIG. 23. Observed intensity as a function of the peak-to-peak voltage applied to the crystal in the linear regime.

REFERENCES

[1] Theresa A. Maldonado . *Handbook of Optics, Volume II - Devices, Measurements, and Properties.* Chap.13 "Electro-Optic Modulators" (1994).

[2] C Langrock, D. Hum, E. Diamanti, M. Charbonneau-Lefort .*High-Speed Optical Modulators.* IEEE Journal of Selected Topics in Quantum Electronics, Vol. XX, No. Y (2002).

[3] J. C. Santos, M. C. Taplamacioglu, K. Hidaka. *Optical high voltage measurement using Pockels microsingle crystal.*The Review of scientific instruments, 70(8):3271-3276 (1999).

[4] M. Bartnick, M. Santandrea, J. P. Hpker, F. Thiele, R. Ricken, V. Quiring, C. Eigner, H. Herrmann, C. Silberhorn and T. J. Bartley. *Cryogenic second harmonic generation in periodically-poled lithium niobate waveguides.* Phys. Rev. Applied 15, 024028 (2021).

[5] M. Abarkan, J.P. Salvestrini, M. Aillerie, M. Fontana. *Frequency dispersion of electro-optical properties over a wide range by means of time-response analysis.* Applied optics, 42 (13), pp.2346-2353 (2003).

[6] A. V. SyuyNikolay, N. ProkopivNikolay, V. SidorovShow, E. A. Antonycheva. *Determination of Electro-Optical Coefficients of Lithium Niobate Crystals.* Key Engineering Materials Vol. 806, 175-179 (2019).

[7] M. Abarkan, A. Danielyan, Sa. Sewastianow, M. Aillerie, N. Théofanous , S. Kostritskii , E. Kokanyan. *The r_{22} electro-optic coefficients in indium-doped congruent lithium–niobate crystals.* NAMES'16 - New Achievements in Materials and Environmental Sciences (2016).

[8] N. A. Mahmoud, N. Nagib, M. S. Bahrawi. *Senarmont Compensator Method Using Inexact $\lambda/4$ Plate.* Mapan - Journal of Metrology Society of India 34(1) (2018).

[9] S. M. Sathikh and G. W. Bigg. *On the Accuracy of Goniometric Compensation Photoelastic Fringe-order Measurements Methods in.* Experimental Mechanics 12, 47–49 (1972).

[10] E. H. Turner. *High-frequency electro-optic coefficients of lithium niobate.* Appl. Phys. Lett. 8, 303 (1966).

[11] Y. Minet, H. Zappe, I. Breunig, K. Buse. *Electro-Optic Control of Lithium Niobate Bulk Whispering Gallery Resonators: Analysis of the Distribution of Externally Applied Electric Fields.* Crystals 11(3), 298 (2021).

[12] A. Roshanghias, G. Bruckner, A. Binder. *LiNbO3 die-attach with Au-Ge eutectic solders.* IEEE CPMT Symposium Japan (ICSJ) (2016).